fluids

MDPI

Article

Thermohydraulic Performance of a Microchannel Heat Sink with Novel Transverse-Section Triangular Ribs: A Parametric Numerical Study

Hazem Meharzi [1], Carlo Nonino [2], El Ghalia Filali [1] and Stefano Savino [2,*]

[1] Faculty of Mechanical and Processes Engineering, Houari Boumediene University, B.P. 32 El Alia, Bab Ezzouar, Algiers 16111, Algeria; hmeharzi@usthb.dz (H.M.); eg_filali@yahoo.fr (E.G.F.)
[2] Dipartimento Politecnico di Ingegneria e Architettura, Università degli Studi di Udine, 33100 Udine, Italy; carlo.nonino@uniud.it
* Correspondence: stefano.savino@uniud.it

Abstract

A three-dimensional conjugate heat-transfer model was used to investigate laminar water flow in a silicon microchannel heat sink equipped with novel staggered transverse-section triangular ribs, whose triangular cross-section is defined directly in the channel transverse plane, normal to the mean flow direction. Simulations were performed for $100 \leq Re \leq 400$ under a uniform base heat flux of 1.0 MW/m^2. Rectangular and triangular ribs were first compared at the same frontal-area blockage ratio, BR = 25%. The rectangular configuration provided a slightly higher performance-evaluation criterion (PEC) up to Re = 200, whereas the triangular configuration became superior at higher Reynolds numbers and yielded an 8.7% higher PEC at Re = 400. A sequential parametric study then examined triangular-rib width, height, blockage distribution, and streamwise spacing. At BR = 37.5% and Re = 400, the full-height/variable-width configuration produced a 55.3% higher Nusselt number and a 30.7% higher PEC than the corresponding full-width/variable-height configuration. Reducing rib spacing from 0.40 to 0.20 mm increased PEC by 74.5%, from 1.37 to 2.40, while the Fanning friction factor increased from 0.118 to 0.279. The complementary heated-base indicators, i.e., overall Nusselt number and PEC_h, confirmed the main performance trends, supporting the conclusion that rib profile, blockage distribution, and spacing jointly govern the thermohydraulic performance of transverse-section triangular-rib microchannels.

Keywords: microchannel heat sink; transverse-section triangular ribs; conjugate heat transfer; blockage ratio; thermohydraulic performance

Check for updates

Academic Editors: Jinyuan Qian and Goncalo Silva

Received: 28 August 2026
Revised: 19 October 2026
Accepted: 27 October 2026
Published: 2 November 2026

Copyright: © 2026 by the authors. Licensee MDPI, Basel, Switzerland. This article is an open access article distributed under the terms and conditions of the Creative Commons Attribution (CC BY) license.

1. Introduction

The continuous increase in power density associated with the miniaturization of electronic devices has intensified the need for compact and efficient thermal-management systems capable of maintaining acceptable operating temperatures and limiting temperature non-uniformity [1–3]. Since the pioneering work of Tuckerman and Pease [4], microchannel heat sinks (MCHSs) have received considerable attention because their high surface-area-to-volume ratio and short conduction paths enable high heat-removal rates within a compact volume. Microscale flow passages and their thermohydraulic characteristics have been extensively classified and discussed in the literature [5], and liquid-cooled MCHSs are now regarded as promising solutions for processors, power electronics, and other high-heat-flux applications [1–3].

Despite their high intrinsic heat-transfer capability, conventional straight microchannels are generally characterized by laminar flow and by the progressive development of hydrodynamic and thermal boundary layers along the channel. Consequently, a wide range of passive enhancement strategies has been investigated. Recent reviews [6,7] classify these approaches into coolant modification and geometric or surface modification.

Working-fluid modification through nanofluids represents one possible route (see, for example, Refs. [8,9]).

A second major class of passive techniques, which is the one considered in this work, consists of modifying the microchannel flow passage itself. Cavities, grooves, expansion–contraction sections, and related interrupted geometries periodically disturb or redevelop the boundary layer and can redirect fluid from the core region toward the heated walls. Pan et al. [10] examined microchannels with different re-entrant cavity shapes and showed that cavity geometry has a direct influence on both heat-transfer augmentation and pressure loss, confirming that the thermal benefit cannot be separated from the way in which the cavity modifies the local flow field. Kumar and Kumar [11] investigated arc grooves placed on the channel floor, on the sidewalls, and on combined surfaces. Their results showed that groove-induced boundary-layer disruption can substantially increase heat transfer. Saha et al. [12] focused specifically on right-triangular grooves machined into the sidewalls and varied the groove angle from 15° to 75° for Reynolds numbers ranging from 100 to 900. The periodic expansion–constriction concept investigated by Chai et al. [13] further demonstrated how repeatedly interrupting the developing flow can reinitialize the hydrodynamic and thermal boundary layers and thereby enhance heat transfer. Overall, these studies establish boundary-layer interruption and redevelopment as one of the recurring physical mechanisms behind passive geometric enhancement in microchannels.

Internal flow promoters provide another route for enhancing single-phase MCHS performance. Micro pin fins increase the wetted area while also producing local acceleration, flow separation, wakes, and secondary motion. Vasilev et al. [14] numerically analyzed seventeen circular pin-fin configurations by varying pin diameter, height, and spacing. Jia et al. [15] investigated oval-shaped micro pin fins for Reynolds numbers ranging from 157 to 668 and independently varied the fin axial-length, width, and height ratios. Ali et al. [16] examined semi-elliptical pin fins with aspect ratios ranging from 0.36 to 1.00 in a silicon MCHS. The fins reduced the heated-wall temperature and enhanced heat transfer, but also increased pressure drop.

Among passive internal promoters, ribs are particularly attractive because their shape, size, location, orientation, porosity, and spacing can be tailored independently of the overall channel dimensions. Li et al. [17] compared solid and porous ribs in middle, symmetrical, and staggered arrangements. Both rib types enhanced heat transfer relative to a smooth channel, but replacing solid ribs with porous ribs significantly reduced the pressure drop. The importance of rib location was highlighted by Ali et al. [18], who mounted trefoil ribs on the base wall, sidewalls, or all walls. Although the all-wall configuration produced the strongest heat-transfer augmentation, its hydraulic penalty reduced the overall benefit. More recently, Ali et al. [19] investigated biomimetic trefoil-shaped cavities located on different microchannel walls, further highlighting the influence of the location of flow-enhancement elements on thermohydraulic performance. Other geometrical enhancement strategies include symmetrical ogive-shaped ribs mounted on different walls [20], NACA 2412 hydrofoil-shaped ribs [21], shark-scale-inspired gradient airfoil ribs [22], and combined structures incorporating inclined ribs, quatrefoil-shaped elements, and elliptical grooves [23]. These studies further highlight the importance of rib geometry and arrangement in determining the balance between heat-transfer enhancement and hydraulic resistance. Dash et al. [24] studied staggered cylindrical ribs with sector angles from 45°

to 80°. Increasing the sector angle progressively increased both Nusselt number and flow resistance. A similar sensitivity to rib orientation was reported for V-shaped ribs by Ali et al. [25]: decreasing the angle of attack from 90° toward 35° intensified heat transfer, but at the cost of a higher friction factor. Wang et al. [26] introduced staggered truncated ribs and varied both rib-height ratio and rib-width ratio for $Re = 223 - 593$. Larger ribs generally increased Nu and friction simultaneously, while truncation could lower the pressure-loss penalty relative to conventional ribs. Additional studies on periodic sidewall modifications [27] and variable-geometry rectangular fins [28] reach the same general conclusion: internal structures can substantially strengthen convection, but their value must be assessed through a combined thermal–hydraulic criterion rather than through heat-transfer enhancement alone.

Direct comparisons among rib shapes provide an important basis for interpreting the influence of geometry, although the configurations adopted in previous studies differ from those considered here. Wang et al. [29] performed an experimental and numerical comparison of rectangular, triangular, and semicircular micro-ribs mounted on opposed sidewalls. Among the tested shapes, the triangular ribs produced the highest Nusselt number but also the highest friction factor. Chai and Wang [30] subsequently compared rectangular, backward-triangular, diamond, forward-triangular, and ellipsoidal ribs located in transverse microchambers within a three-dimensional conjugate heat-transfer model, showing that the ranking of rib shapes depends on the operating range and on the balance between heat transfer and pressure loss. Wang et al. [31] also compared interrupted microchannels without ribs and with rectangular, triangular, and trapezoidal ribs over Reynolds numbers ranging from 100 to 900. In that study, the rectangular rib produced the largest increases in both average Nusselt number and friction factor, whereas the trapezoidal rib provided the highest overall PEC. These studies demonstrate that the ranking of rib shapes depends on the balance between heat-transfer enhancement and hydraulic penalty and, importantly, on the specific geometric framework in which the comparison is performed.

Triangular ribs deserve a more specific discussion because their inclined faces can redirect the core flow, accelerate the fluid through locally restricted regions, promote impingement on downstream surfaces, and repeatedly interrupt the thermal boundary layer, while the wake region may exhibit separation and recirculation. However, the term "triangular rib" has been used in the micro/minichannel literature for geometrically different concepts. Wong and Lee [32] investigated triangular ribs located inside transverse microchambers and independently varied rib width, length, and height. In their configuration, the triangular planform develops in a plane parallel to the channel base. They found that heat transfer increased as rib width and height increased, whereas increasing rib length was less favourable. Chai et al. [33,34] considered triangular ribs mounted on the parallel sidewalls in aligned and offset arrangements. In their configuration, the triangular or saw-tooth profile is likewise defined in the plane parallel to the channel base, while the parameter denoted as rib height represents the lateral protrusion into the flow passage and is normalized with the channel width rather than with the channel height. Depending on geometry and arrangement, the average Nusselt number increased up to 2.16 times that of the straight reference channel, while the friction factor could increase by as much as about nine times.

Further studies confirm the strong sensitivity of triangular enhancement elements to their orientation and dimensional ratios. Chen et al. [35] investigated regular triangular prisms in a minichannel by varying prism orientation, height, and transverse offset. The backward-oriented triangular prism provided the most favourable overall response for most of the investigated conditions; however, the triangular prism is a three-dimensional obstruction whose triangular planform and orientation differ from the frontal cross-section

adopted in the present work. Feng et al. [36] investigated staggered triangular ribs in a 0.2 mm × 0.2 mm microchannel, varying rib width, height, and length. The rib height ranged from 0.012 to 0.072 mm, confirming that partial-height triangular ribs have already been considered in the microchannel literature. Increasing relative width and height improved heat transfer but also increased resistance. Alnaimat et al. [37] examined triangular ribs located on the sidewalls and quantified the effects of rib dimensions and pitch in terms of thermal resistance, pumping power, and figure of merit; reductions in pitch decreased thermal resistance but increased the pumping requirement. Shamsoddini Lori and Vafai [38] compared periodic solid and porous ribs of several shapes, including isosceles, forward-triangular, and backward-triangular geometries, and investigated the effects of rib height and porous-medium parameters. Collectively, these studies establish that triangular-rib width, height, length, spacing, orientation, arrangement, and partial-height configurations have already been investigated in micro- and minichannels. They also show, however, that the geometric meaning and orientation of the triangular profile differ substantially among the available configurations.

The extensive literature on rib-roughened channels at conventional scales provides an additional framework for interpreting the transport mechanisms induced by ribs. Han et al. [39] demonstrated that rib shape, angle of attack, and pitch-to-height ratio strongly affect both heat transfer and friction, while Ling et al. [40] showed that triangular ribs can produce substantial heat-transfer enhancement, albeit with a pronounced pressure-drop penalty. Ahn [41], through a direct comparison among different roughness geometries, similarly reported particularly high heat-transfer performance for triangular ribs. These studies support the interpretation of rib-induced enhancement in terms of boundary-layer disruption, flow separation and reattachment, secondary motion, and form drag. Webb [42] further established performance-evaluation criteria for assessing enhanced heat-transfer surfaces under combined thermal and hydraulic constraints. Nevertheless, quantitative results and optimum geometric ratios obtained at conventional scales cannot be transferred directly to microchannels. Wang et al. [43] demonstrated that, although similar rib-induced flow structures may persist across different scales, both Nusselt number and friction characteristics exhibit scale-dependent behaviour. Accordingly, macroscale studies are used here primarily to support the physical interpretation of the observed mechanisms rather than as direct quantitative benchmarks.

Within the micro/minichannel literature examined in the present review [29–38], triangular ribs have been investigated with different orientations, dimensional ratios, and arrangements. However, no study was identified in which the triangular cross-section of the rib is defined directly in the channel transverse plane, normal to the mean streamwise flow, so that the triangular area constitutes the frontal obstruction of the channel cross-section. This geometrical distinction is central to the present investigation, since rib width and height determine not only the magnitude of the frontal obstruction but also its spatial distribution within the channel cross-section. In particular, the same frontal-area blockage ratio can be obtained with different combinations of rib width and height, resulting in geometrically distinct configurations. Although previous studies have examined the effects of rib dimensions and shape, the influence of the spatial distribution of an identical frontal obstruction has not been systematically investigated for this type of triangular rib. To the best of the authors' knowledge, a systematic comparison of transverse-section triangular ribs at matched frontal-area blockage ratios has not been reported in the reviewed literature.

The main contribution of the present study is a systematic thermohydraulic investigation of transverse-section triangular ribs, with particular emphasis on comparisons at matched frontal-area blockage ratios. This approach makes it possible to distinguish the effects of rib shape and spatial distribution of the frontal obstruction from those associated

with the blockage magnitude itself. In the first stage, rectangular and triangular ribs are compared at the same frontal-area blockage ratio, in order to assess the effect of rib shape while maintaining the same fraction of obstructed channel cross-sectional area. This initial comparison also provides a complementary basis for comparison with previous studies addressing rectangular and triangular-rib geometries [29–31], while adopting a different geometric constraint and a different orientation of the triangular section. Based on the results of this preliminary comparison, the triangular configuration is subsequently retained for the parametric investigation. Rib width is first varied while maintaining the full channel height, after which rib height is varied while maintaining the full channel width; the resulting full-height/variable-width and full-width/variable-height families form paired configurations at matched-blockage ratios. This design permits the influence of the spatial distribution of an identical frontal obstruction to be examined independently of the blockage ratio itself. Finally, rib spacing is varied for the selected triangular configuration. The study therefore provides a comprehensive assessment of the effects of rib geometry on thermohydraulic performance over the Reynolds number range of 100 to 400. In addition to conventional thermal and hydraulic indicators, complementary performance criteria based on the heated-base temperature and field-synergy analysis are employed to provide further insight into the effectiveness of the investigated configurations.

2. Statement of the Problem and Numerical Methodology

The present study considers three-dimensional laminar forced convection of water in a silicon microchannel heat sink subjected to a uniform heat flux at its bottom surface. The microchannel has a rectangular cross-section, while staggered ribs are introduced into the flow passage to enhance fluid mixing and periodically disturb the developing thermal boundary layer.

The investigation is structured as a sequential parametric study. First, a smooth microchannel and two ribbed configurations, incorporating rectangular and triangular ribs, are compared. The rectangular and triangular ribs are designed at the same frontal-area blockage ratio, so that the influence of rib shape can be assessed under the same degree of cross-sectional obstruction. Based on this preliminary comparison, the triangular-rib configuration is retained for the subsequent parametric analysis. The triangular ribs considered in this work have a triangular cross-section defined directly in the plane transverse to the mean flow direction. Their height, width, and streamwise spacing are varied systematically, while their thickness is kept constant. Two geometric families are examined: full-height ribs with variable width and full-width ribs with variable height. These configurations also provide matched frontal-area blockage ratios, enabling the influence of the spatial distribution of the obstruction within the channel cross-section to be distinguished from that of the blockage magnitude itself. Finally, the effect of rib spacing is investigated while maintaining the selected rib height and width.

The thermal and hydraulic responses are evaluated in terms of average heated-wall temperature, Nusselt number, Fanning friction factor, and performance-evaluation criterion (PEC). The numerical formulation, computational domains, boundary conditions, solution procedure, and definitions of the performance parameters are presented in the following subsections.

2.1. Mathematical Model and Governing Equations

Three-dimensional conjugate heat transfer in a single silicon microchannel was numerically investigated, accounting for both heat conduction through the silicon substrate and ribs and convection within the coolant. The following assumptions were adopted:

(1) The fluid is single-phase, incompressible, and Newtonian.

(2) The flow is steady and laminar over the investigated Reynolds-number range.
(3) Thermophysical properties of water and silicon are constant.
(4) No-slip conditions apply at all fluid–solid interfaces, and perfect thermal contact is assumed between water and silicon.
(5) Radiation, body forces, and heat exchange with the external environment are neglected.
(6) Viscous dissipation is neglected.

The single-phase flow assumption is consistent with the intended application to electronic cooling, for which the predicted operating temperatures remain well below the saturation temperature of water under the considered pressure conditions.

Under these assumptions, the governing equations are the continuity, the Navier–Stokes and the thermal energy equation in the fluid domain

$$\nabla \cdot \boldsymbol{u} = 0 \tag{1}$$

$$\rho_f \boldsymbol{u} \cdot \nabla \boldsymbol{u} = -\nabla p + \mu_f \nabla^2 \boldsymbol{u} \tag{2}$$

$$\rho_f C_{pf} \boldsymbol{u} \cdot \nabla T = k_f \nabla^2 T \tag{3}$$

and the thermal conductivity equation in the solid

$$k_s \nabla^2 T = 0 \tag{4}$$

In the above equations, $\boldsymbol{u}$ is the velocity vector, p is the static pressure, and T is the temperature, ρ_f denotes the fluid density, μ_f the dynamic viscosity, k_f and C_{pf} the fluid thermal conductivity and specific heat capacity at constant pressure, respectively, while k_s is the silicon thermal conductivity. At every water–silicon interface, continuity of temperature and normal heat flux is imposed.

It must be pointed out that, since the main purpose of the study is to compare the effects of different geometrical configurations, constant properties were deliberately adopted to isolate the effect of geometry without introducing an additional temperature-dependent contribution to the observed differences. Furthermore, as will be clarified later, most of the simulations were performed based on a periodic computational approach that imposes practical limitations on the use of temperature-dependent properties in the numerical formulation. All the thermophysical properties were evaluated at a temperature of 300 K. Their values are: $\rho_f = 998.2$ kg/m^3, $\mu_f = 0.001003$ Pa·s, $k_f = 0.6$ W/(m·K), $C_{pf} = 4182$ J/(kg·K), and $k_s = 148$ W/(m·K).

2.2. Computational Domains and Boundary Conditions

Figure 1 shows the full-length computational domain used to represent a single microchannel and the surrounding silicon substrate. The overall dimensions of the model are length $L = 10$ mm, height $H = 0.35$ mm and width $W = 0.25$ mm. The internal flow passage has an unobstructed microchannel width $W_{ch} = 0.10$ mm and an unobstructed microchannel height $H_{ch} = 0.20$ mm, corresponding to a cross-sectional area $A_{ch} = W_{ch}H_{ch} = 0.020$ mm^2 and a hydraulic diameter $D_h = 2W_{ch}H_{ch}/(W_{ch} + H_{ch}) = 0.1333$ mm.

The triangular ribs are characterized by a triangular frontal cross-section defined directly in the channel transverse plane, as shown in Figure 2a. Rib height h and width w therefore determine the area projected normal to the mean flow direction. The triangular cross-section was extruded over a constant streamwise rib thickness $t_{rib} = 0.05$ mm for all configurations. The percentage frontal-area blockage ratio is defined as

$$\mathrm{BR} = 100\frac{A_{rib}}{A_{ch}} \tag{5}$$

where A_{rib} is the projected rib area and A_{ch} is the unobstructed channel cross-sectional area. For the triangular ribs, $A_{rib} = h\,w/2$ whereas for the rectangular rib, $A_{rib} = h\,w$.

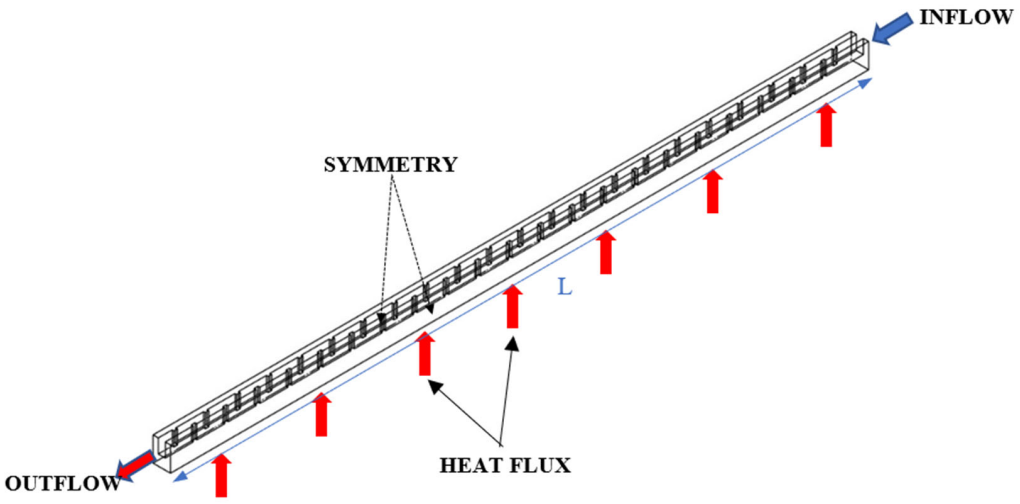


Figure 1. Full-length computational domain with boundary conditions.

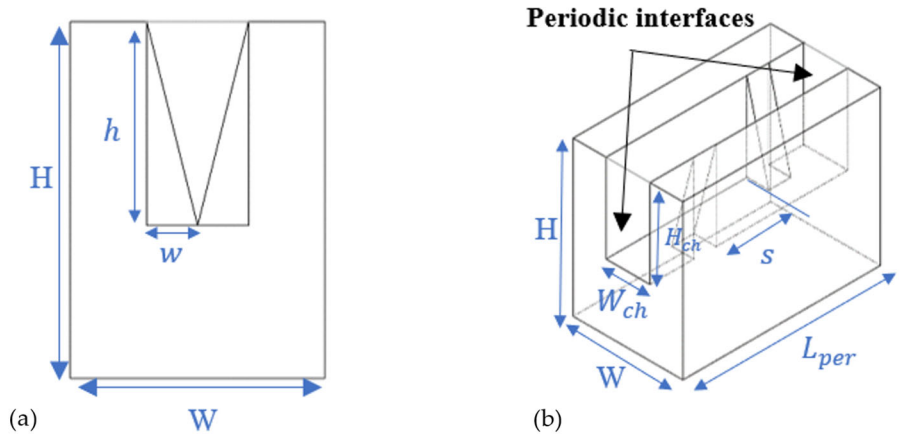


Figure 2. Front view showing the dimensions of the MCHS (**a**), and three-dimensional view of the periodic computational module with dimensions and boundary conditions (**b**).

To reduce the computational cost of the parametric investigation, the repeated ribbed region was represented by a periodic computational module with length L_{per} containing two staggered ribs, as illustrated in Figure 2b.

The investigated configurations illustrated in Figure 3 and summarized in Table 1 were selected according to a sequential parametric approach, aimed at progressively investigating the effects of rib shape, width, height, and spacing. Particular attention was given to identifying pairs of configurations with the same frontal-area blockage ratio but different rib dimensions, allowing the influence of the spatial distribution of the obstruction to be assessed. The adopted nomenclature, described below, reflects the geometric parameters varied in the investigation, while the rationale behind the selection of the different configurations is further discussed through the comparative analysis of the results presented in Section 4.

A total of ten configurations were considered: one smooth microchannel, hereafter denoted as "smooth"; one microchannel equipped with rectangular ribs, denoted as "rect"; and eight configurations incorporating triangular ribs.

The triangular-ribbed configurations are identified using the compact notation "h*i*w*j*s*k*", where the letters h, w, and s refer to rib height, rib width, and rib spacing, respectively, and the integers *i*, *j* and *k* identify the corresponding geometric level. For rib

height and width, the numerical indices i and j represent fractions of the unobstructed microchannel height H_{ch} and width W_{ch}. Specifically,

$$h = \frac{i}{4}H_{ch}, \quad w = \frac{j}{4}W_{ch} \tag{6}$$

with $i, j = 1, 2, 3, 4$, corresponding to 25%, 50%, 75%, and 100% of the channel height or width, respectively. Thus, for example, h4w2s1 denotes a triangular rib extending over the full channel height ($h = H_{ch}$) and one-half of the channel width ($w = 0.5W_{ch}$). The spacing index k does not represent a geometric fraction, but identifies one of the three investigated streamwise rib spacings: s1, s2, and s3, corresponding to $s = 0.20$, 0.30, and 0.40 mm, respectively. This notation provides a concise means of identifying each configuration while clearly distinguishing the independent variations in rib height, width, and spacing.

Table 1. Geometrical parameters of the studied designs.

Configuration	L_{per} [mm]	h [mm]	w [mm]	s [mm]	BR [%]
smooth	0.45	0	0	0	-
rect	0.45	0.20	0.025	0.2	25.0
h4w1s1	0.45	0.20	0.025	0.2	12.5
h4w2s1	0.45	0.20	0.050	0.2	25.0
h4w3s1	0.45	0.20	0.075	0.2	37.5
h1w4s1	0.45	0.05	0.100	0.2	12.5
h2w4s1	0.45	0.10	0.100	0.2	25.0
h3w4s1	0.45	0.15	0.100	0.2	37.5
h4w3s2	0.65	0.20	0.075	0.3	37.5
h4w3s3	0.85	0.20	0.075	0.4	37.5

For the full-length domain, a uniform inlet velocity was imposed and adjusted to obtain the prescribed Reynolds number, while the inlet water temperature was fixed at 300 K. A pressure-outlet boundary condition with a gauge pressure of 0 Pa was imposed at the channel exit. A uniform heat flux of $q_h = 10^6$ W/m^2 was applied to the bottom surface of the silicon substrate. Symmetry conditions were imposed on the external lateral planes of the silicon domain, representing an idealized array of adjacent microchannels operating under identical thermal and hydraulic conditions. Such an arrangement may be realized by placing neighbouring microchannels in a mirror-symmetric configuration, even when the ribs within each individual channel are staggered. The remaining external silicon surfaces were treated as adiabatic. At the water–silicon interfaces, including the rib surfaces, no-slip and thermally coupled boundary conditions were imposed, ensuring continuity of temperature and heat flux across the interface. For the reduced computational modules, the two streamwise end planes, identified as periodic interfaces in Figure 2b, were defined as a translational periodic pair. The imposed flow rate was selected so that the Reynolds number, based on the unobstructed channel cross-sectional area and the reference hydraulic diameter D_h, matched the corresponding full-domain condition, and the bulk temperature on the inlet periodic interface was set to 300 K. For the periodic simulations, the mass flow rate corresponding to the prescribed Reynolds number was imposed, while no inlet or outlet pressure values were explicitly specified. Instead, ANSYS Fluent 2025R1 automatically determined the mean streamwise pressure gradient required to maintain the prescribed mass flow rate [44].

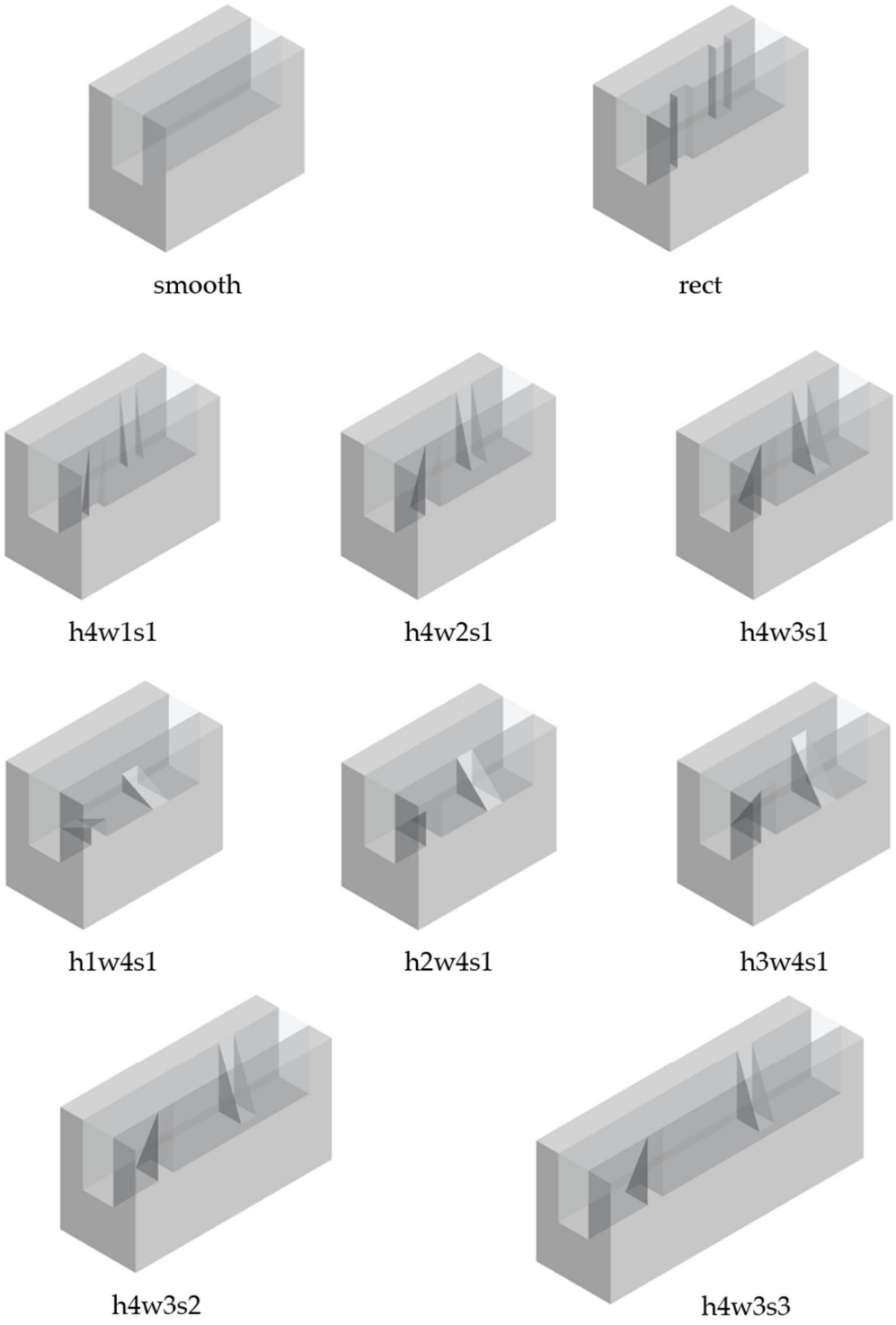


Figure 3. Configurations of the investigated periodic MCHS modules.

2.3. Solution Methods and Convergence Criteria

The governing equations were solved using the finite-volume method implemented in ANSYS Fluent 2025R1 [44], using double precision. Pressure–velocity coupling was performed using the coupled algorithm. Spatial discretization of the momentum and energy equations was performed using second-order upwind schemes. The normalized residual convergence criteria were set to 10^{-6} for continuity and momentum and to 10^{-9} for the energy equation. Residual convergence alone was not considered sufficient; the

solution was accepted only after monitored integral quantities, including pressure drop and characteristic fluid/wall temperatures, had reached steady values.

2.4. Data Reduction

Several parameters were used to characterize the flow and heat-transfer behaviour within the MCHS studied. The Reynolds number is defined as $\mathrm{Re} = \rho_f u_m D_h / \mu_f$, where u_m is the mean velocity based on the unobstructed channel cross-section and D_h is the hydraulic diameter of the smooth channel. The same reference hydraulic diameter is used for all ribbed configurations.

The average Fanning friction factor was calculated from the pressure drop along the computational domain as $f = D_h \Delta p_{per} / \left(2\, L_{per} \rho_f u_m^2\right)$, where Δp_{per} is the pressure loss over the periodic module and L_{per} is the corresponding module length. For the full-length validation model, L is used instead of L_{per}.

The average heat-transfer coefficient was determined using the relation

$$\alpha = \frac{q_h A_h}{A_{sf}\left(T_{sf} - T_b\right)} \tag{7}$$

where A_h is the externally heated silicon base area, A_{sf} is the total water–silicon heat-transfer interface within the evaluation domain, T_{sf} is its area-weighted mean temperature, and T_b is the representative bulk temperature, calculated as the average between mass-weighted inlet and outlet temperatures on the considered domain. The corresponding average Nusselt number was evaluated as $\mathrm{Nu} = \alpha D_h / k_f$.

The conventional average heat-transfer coefficient α is based on the actual fluid–solid interfacial area A_{sf} which varies with rib geometry. Consequently, an increase in this area reduces the average heat flux per unit interfacial area for a given total heat-transfer rate, without necessarily implying a reduction in the overall cooling effectiveness. To account for this aspect, a complementary overall heat-transfer coefficient α_h is introduced using the fixed heated-base area A_h and the temperature difference $T_h - T_b$, where T_h is the area-weighted mean temperature of the externally heated silicon base

$$\alpha_h = \frac{q_h}{T_h - T_b} \tag{8}$$

The corresponding overall Nusselt number $\mathrm{Nu}_h = \alpha_h D_h / k_f$ reflects the combined effects of conduction through the silicon structure and convection to the coolant, without explicitly depending on A_{sf}. Thus, while Nu characterizes the average convective performance at the fluid–solid interface, Nu_h provides a complementary measure of the overall heat sink effectiveness in cooling the heated surface, allowing a better comparison of the performances yielded by different geometries.

To compare the performance of the enhanced microchannels with the smooth baseline, the performance-evaluation criterion (PEC) was calculated as follows [42]:

$$\mathrm{PEC} = \frac{\mathrm{Nu}}{\mathrm{Nu}_0} \Big/ \left(\frac{f}{f_0}\right)^{1/3} \tag{9}$$

where Nu_0 and f_0 refer to the smooth microchannel at the same Reynolds number. The exponent provides the conventional equivalent-pumping-power comparison for geometrically similar channels.

The performance-evaluation criterion yielded by the overall heat-transfer coefficient defined by Equation (8) is

$$\mathrm{PEC}_h = \frac{\mathrm{Nu}_h}{\mathrm{Nu}_{h,0}} \Big/ \left(\frac{f}{f_0}\right)^{1/3} \tag{10}$$

where Nu_h and $Nu_{h,0}$ refer to the ribbed and smooth channel, respectively. The comparison between PEC and PEC_h makes it possible to assess whether the thermohydraulic advantages identified using the conventional Nusselt number are also retained when the performance evaluation is referred to the heated surface. This distinction is particularly relevant for configurations with different rib dimensions and spacings, which modify both the fluid–solid contact area and the flow structures responsible for heat-transfer enhancement.

The energy transfer process in a MCHS can also be assessed using parameters based on the Field-Synergy Principle, such as the local synergy angle between the velocity vector and the temperature gradient [45,46]

$$\beta = \cos^{-1}\left(\frac{\boldsymbol{u}\cdot\nabla T}{|\boldsymbol{u}|\,|\nabla T|}\right) \tag{11}$$

and domain integration mean synergy angle [45,46]

$$\beta_m = \cos^{-1}\left(\frac{\int_{\boldsymbol{\Omega}} \boldsymbol{u}\cdot\nabla T\, d\Omega}{\int_{\boldsymbol{\Omega}} |\boldsymbol{u}|\,|\nabla T|\, d\Omega}\right) \tag{12}$$

where Ω represents the fluid domain.

3. Grid Independence and Model Validation

Before performing the parametric analysis, the numerical methodology was assessed through a grid-independence study and three complementary validation steps. These included comparison with experimental data for a smooth microchannel, comparison with published numerical results for a ribbed microchannel, and verification of the reduced periodic-domain approach against the corresponding full-length model.

3.1. Grid-Independence Study

An unstructured tetrahedral mesh was employed throughout the computational domain, with local refinement near the fluid–solid interfaces and rib surfaces to adequately resolve the velocity and temperature gradients. Grid-independence studies were carried out at Re = 300 for three representative configurations: the smooth microchannel, the rectangular-ribbed microchannel, and the triangular-ribbed configuration h4w2s1. The latter two configurations were selected to assess mesh sensitivity in the presence of different rib geometries. Five progressively refined meshes were examined for each configuration, monitoring the average Nusselt number Nu and the Fanning friction factor f.

The relative percentage error between the value of the parameter obtained using a coarser mesh i and the value obtained with the finest mesh was calculated using the following expression:

$$e_{\emptyset} = \left|\frac{\emptyset_{finest} - \emptyset_i}{\emptyset_{finest}}\right| \cdot 100 \tag{13}$$

where $\emptyset$ denotes either Nu or f, $\emptyset_i$ is the value obtained with the considered mesh, and $\emptyset_{finest}$ is the value obtained using the finest mesh. For the smooth microchannel, the relative differences between the two finest meshes were only 0.35% for Nu and 0.15% for f. Since the ribbed configurations involve more complex flow and temperature fields, only their grid-refinement results are reported in Table 2. Comparing the adopted fourth mesh with the fifth (finest) mesh gives relative differences of 0.78% in Nu and 0.21% in f for rect, and 0.27% in Nu and 0.25% in f for h4w2s1. The fourth mesh was therefore selected as a compromise between computational cost and mesh sensitivity. The final mesh is depicted in Figure 4 for the rectangular-ribbed channel. The same meshing strategy, including local refinement near solid–fluid interfaces and ribs, was applied to the other configurations, adjusting the mesh density to their geometries.

Table 2. Grid-independence study for the rectangular and triangular-ribbed MCHSs at Re = 300. Differences are relative to the finest mesh of each configuration.

Configuration	Number of Cells	f [−]	e_f (%)	Nu [−]	e_{Nu}[%]
Rectangular	15,808	0.11822	6.96	13.641	33.85
	340,676	0.11180	1.15	10.651	4.51
	643,676	0.11114	0.55	10.430	2.35
	1,272,848	0.11076	0.21	10.270	0.78
	2,570,511	0.11053	Baseline	10.191	Baseline
h4w2s1	42,680	0.12215	7.39	11.468	7.71
	365,420	0.11684	2.73	10.936	2.71
	748,350	0.11504	1.14	10.781	1.26
	1,486,720	0.11403	0.25	10.676	0.27
	2,964,580	0.11374	Baseline	10.647	Baseline

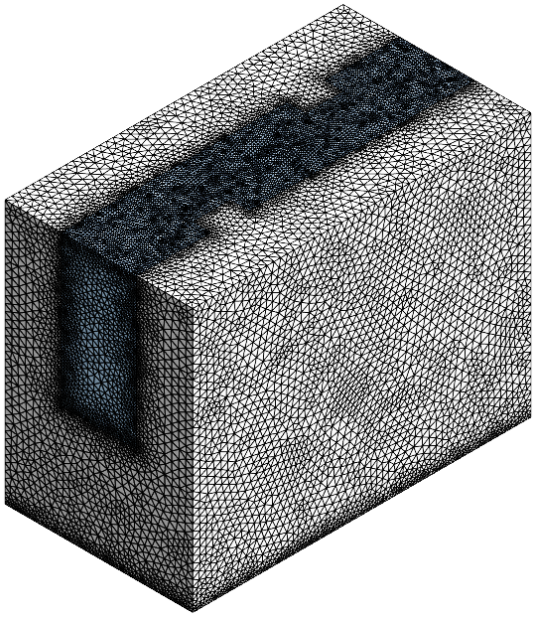


Figure 4. Computational mesh of the rectangular-ribbed MCHS.

To complement the conventional grid-independence analysis, the numerical discretization uncertainty was estimated using the Grid Convergence Index (GCI) method proposed by Roache [47]. The analysis was performed using Meshes 2, 3, and 4, with refinement ratios estimated from the total number of computational cells and a safety factor of 1.25. The apparent orders of convergence were 1.77 and 2.84 for Nu and f, respectively, in the rectangular-ribbed configuration, and 1.48 and 2.28 in the triangular-ribbed configuration. The corresponding GCI values for the adopted fourth mesh were 3.94% for Nu and 0.47% for f for the rectangular-ribbed configuration, and 3.05% for Nu and 1.62% for f for the triangular-ribbed configuration. These results, together with the small variations observed upon further mesh refinement, support the selection of Mesh 4 as a reasonable compromise between discretization uncertainty and computational cost.

3.2. Validation for the Smooth MCHS

The numerical methodology was first validated against the experimental data reported by Chai et al. [13] for a smooth microchannel. The reference geometry and operating conditions were reproduced according to the original study. Figure 5 compares the present predictions with the published results in terms of Nusselt number and Fanning friction factor.

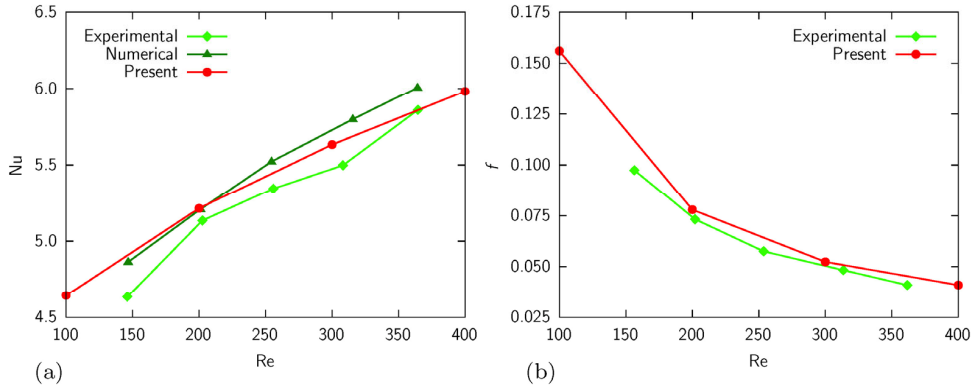


Figure 5. Comparison of the present numerical predictions with the numerical and experimental results of Chai et al. [13]: Nusselt number (**a**) and Fanning friction factor (**b**).

As shown in Figure 5a, the predicted Nusselt numbers reproduce both the magnitude and the Reynolds-number dependence of the experimental data. Based on linear interpolation of the experimental data at the Reynolds numbers simulated in the present study, the mean absolute relative deviation is 2.08%, with a maximum deviation of 2.90%. Figure 5b shows similarly satisfactory agreement for the Fanning friction factor, with a mean absolute relative deviation of 5.30% and a maximum deviation of 7.09%. These results indicate that the adopted numerical methodology provides an adequate prediction of both heat-transfer and hydraulic behaviour for the smooth microchannel.

3.3. Validation for the Ribbed MCHS

A second validation was performed to assess the capability of the numerical model to reproduce heat transfer and pressure losses in the presence of internal ribs. The geometry and operating conditions reported by Li et al. [17] were reproduced, and the present predictions were compared with their numerical results in terms of maximum base-wall temperature and pressure drop.

Figure 6a shows excellent agreement for the maximum wall temperature, with a mean absolute relative deviation of 0.12% and a maximum deviation of 0.30%. The pressure-drop comparison reported in Figure 6b also shows satisfactory agreement. The mean absolute relative deviation is 3.97%, while the largest discrepancy, 12.61%, occurs at the lowest investigated Reynolds number, Re = 80. Excluding this point, the mean pressure-drop deviation decreases to 1.81%. Overall, the agreement obtained for both thermal and hydraulic quantities provides additional support for the applicability of the present numerical approach to ribbed microchannels.

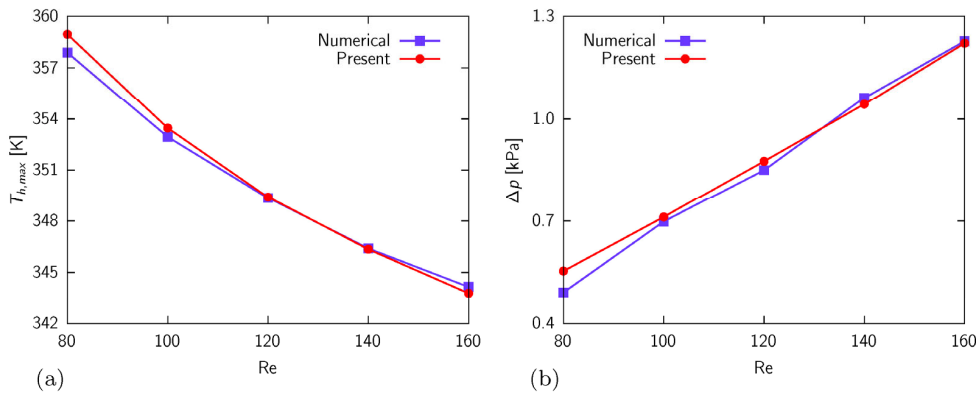


Figure 6. Comparison of the present numerical predictions with the numerical results of Li et al. [17]: maximum base-wall temperature T_{max} (**a**) and pressure drop Δp (**b**).

3.4. Validation of the Periodic-Domain Approach

Since the parametric investigation was performed using reduced periodic computational modules, the periodic-domain approach was independently assessed against the corresponding full-length microchannel model. For this purpose, the comparison was not based on quantities averaged over the entire full-length channel, since these would also include the developing entrance region. Instead, the Nusselt number and Fanning friction factor were evaluated over a downstream section located near the outlet of the full-length domain, where entrance effects are substantially reduced, and the flow and thermal fields approach their developed behaviour.

The results obtained over this downstream evaluation section were then compared with those predicted by the periodic computational module under the same Reynolds number, fluid properties, and applied heat flux. The downstream evaluation section had the same streamwise length as the corresponding periodic module, so that the two sets of quantities were evaluated over equivalent axial extents.

Figure 7 compares the Fanning friction factor and Nusselt number obtained from the periodic module, referred to as "periodic domain" in the figure, with those evaluated over the downstream section of the full-length model, referred to as "small portion of the domain" in the figure. The Nusselt-number predictions show very close agreement over the entire Reynolds-number range, with a mean absolute relative deviation of 0.70% and a maximum deviation of 1.40%. The corresponding Fanning friction factor has a mean absolute relative deviation of 1.59%, with a maximum deviation of 2.57%. These results indicate that the periodic computational module adequately reproduces the thermohydraulic behaviour observed in the downstream region of the full-length channel while substantially reducing the computational cost. The periodic-domain approach was therefore adopted for the subsequent parametric investigation.

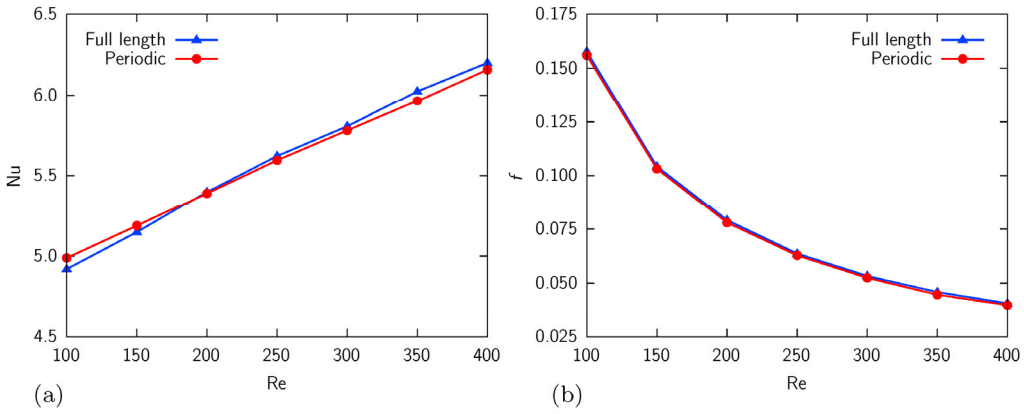


Figure 7. Validation of the periodic-domain approach by comparison with quantities evaluated over the downstream section of the full-length microchannel: Fanning friction factor (**a**) and Nusselt number (**b**).

4. Results and Discussion

The numerical results are presented and discussed in this section with the aim of clarifying the influence of rib geometry on the thermal and hydraulic behaviour of the microchannel heat sink. The analysis first focuses on the effect of rib shape through the comparison between the smooth, rectangular-ribbed, and triangular-ribbed configurations. The influence of the main geometric parameters of the transverse-section triangular ribs is then examined by varying rib width and height, followed by a direct comparison of configurations having matched frontal-area blockage ratios. Finally, the effect of rib spacing is assessed for the best-performing triangular configuration identified within the investi-

gated parameter range. The discussion considers both thermal enhancement and hydraulic penalty through the combined analysis of wall temperature, Nusselt number, Fanning friction factor, and PEC.

4.1. Effect of Rib Shape: Comparison of Smooth, Rectangular, and Triangular Microchannels

The first stage of the investigation examines the effect of rib shape by comparing the smooth microchannel with the rectangular-ribbed configuration (rect) and the transverse-section triangular-ribbed configuration h4w2s1. The rectangular and triangular ribs were designed with the same frontal-area blockage ratio, BR = 25%. Therefore, both configurations obstruct the same fraction of the unobstructed channel cross-sectional area, providing a controlled basis for assessing the influence of rib profile on the resulting thermal and hydraulic behaviour.

To examine the flow and thermal mechanisms associated with the different geometries, Figures 8–10 present the velocity and temperature fields at the highest investigated Reynolds number, Re = 400. The flow direction is always from right to left. On the left, the velocity magnitude and velocity vectors are shown on two horizontal planes located at $z = 0.22\ H_{ch}$ and $z = 0.78\ H_{ch}$, hereafter referred to as the lower and upper planes, respectively. These two locations were selected to highlight the different flow disturbances induced by the rib geometry across the channel height. On the right, the temperature distribution on the fluid–solid interface, i.e., the microchannel walls, is reported.

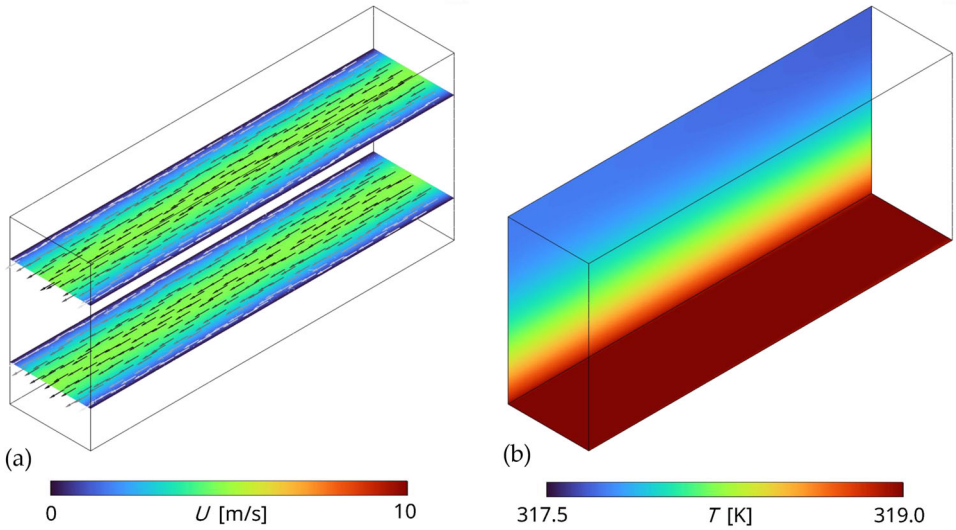


Figure 8. Velocity and temperature fields for the smooth MCHS at Re = 400: velocity-magnitude contours with velocity vectors (**a**); temperature distribution on the microchannel walls (**b**).

In the smooth microchannel (Figure 8), the velocity field remains regular and symmetric, with the highest velocities concentrated in the central portion of the channel. The absence of internal flow promoters allows the thermal boundary layer to develop without periodic disruption, resulting in the highest wall temperatures among the three configurations.

The introduction of rectangular ribs substantially modifies the flow field (Figure 9). The fluid is accelerated around the obstruction, while low-velocity recirculation regions develop downstream of each rib. Because the rectangular rib spans the full channel height, comparable disturbances are observed on the two horizontal planes considered. These repeated separation and reattachment processes modify the local thermal field and interrupt the progressive development of the near-wall thermal boundary layer.

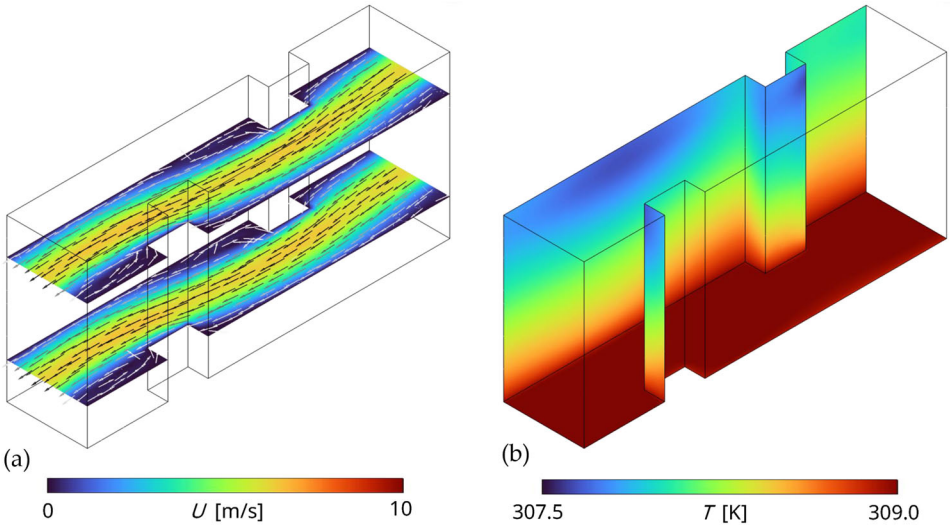


Figure 9. Velocity and temperature fields for the rectangular (rect) MCHS at Re = 400: velocity-magnitude contours with velocity vectors (**a**); temperature distribution on the microchannel walls (**b**).

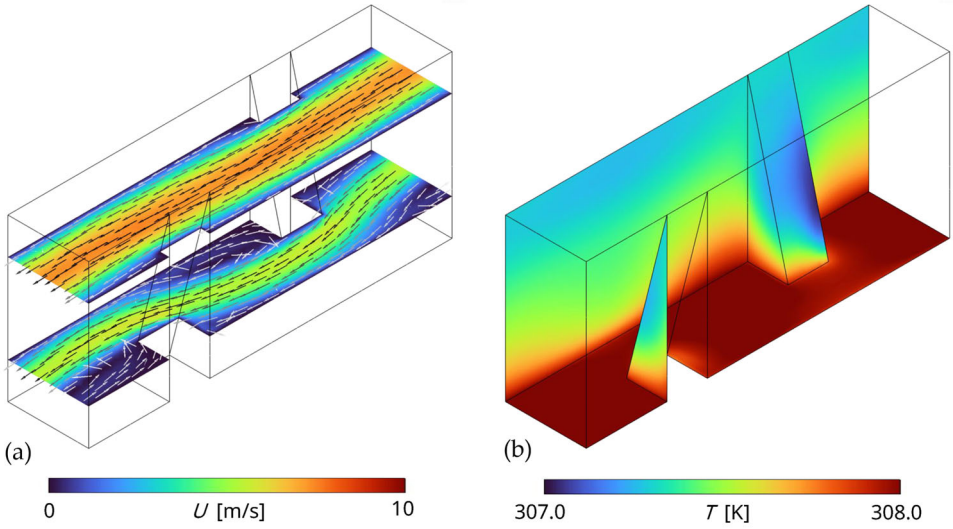


Figure 10. Velocity and temperature fields for the h4w2s1 MCHS at Re = 400: velocity-magnitude contours with velocity vectors (**a**); temperature distribution on the microchannel walls (**b**).

A different flow redistribution is observed for the transverse-section triangular ribs (Figure 10). Owing to the variation in rib width along the channel height, the obstruction imposed on the flow is inherently non-uniform in the vertical direction. The lower plane, where the triangular rib occupies a larger fraction of the local passage width, exhibits stronger flow deflection and a more pronounced downstream recirculation region, whereas the upper plane remains comparatively less disturbed. The triangular geometry therefore generates a vertically non-uniform redistribution of momentum that differs fundamentally from that produced by the full-height rectangular rib, despite the identical frontal-area blockage ratio.

The corresponding temperature field also reflects this difference. Both ribbed configurations reduce the wall temperature relative to the smooth channel, but the triangular ribs produce a more marked local redistribution of the thermal field around the rib surfaces and in their downstream regions. From Figure 10b, it can be observed that, for triangular ribs, the minimum temperature regions are located on the rib surfaces rather than on the channel walls. This behaviour can be attributed to the local impingement of relatively cooler

fluid redirected towards the inclined triangular-rib surfaces, as suggested by the velocity vectors in Figure 10a. The resulting local enhancement of convective heat transfer produces a non-uniform temperature distribution along the rib height and modifies the temperature gradients on the fluid–solid interface. The observed mechanisms are qualitatively consistent with previous studies of ribbed microchannels, in which heat-transfer enhancement has been associated with flow separation, wake formation, fluid redistribution, and repeated disruption and redevelopment of the thermal boundary layer [29,30,33,34]. However, direct quantitative comparison with those studies is not appropriate because the triangular profiles considered therein differ in orientation and geometric definition from the transverse-section ribs investigated here.

Figure 11 provides the quantitative comparison in terms of average heated-wall temperature, Nusselt number, Fanning friction factor, and PEC. The average wall temperature decreases with increasing Reynolds number for all configurations (Figure 11a), as expected from the increased coolant flow rate. Both ribbed channels maintain lower wall temperatures than the smooth reference over the entire investigated range. At lower Reynolds numbers, the rectangular-ribbed configuration provides slightly lower wall temperatures than h4w2s1; however, the difference progressively decreases, and the triangular-ribbed configuration becomes thermally more effective as the Reynolds number increases. At Re = 400, the average wall temperature is approximately 320 K for the smooth channel and about 310 and 309 K for the rectangular and triangular configurations, respectively. A similar behaviour is observed for the Nusselt number (Figure 11b). The smooth microchannel exhibits a relatively weak dependence of the Nusselt number on Reynolds number, whereas the ribbed configurations show a much more pronounced increase in Nu as Reynolds number increases. At Re = 400, Nu increases from 6.16 for the smooth channel to 12.73 for the rectangular-ribbed case and 14.23 for h4w2s1. These values correspond to Nusselt number enhancements of 106.7% and 131.0%, respectively, compared to the smooth microchannel. The rectangular rib provides a marginally higher Nusselt number at lower Reynolds numbers, whereas the triangular rib becomes increasingly advantageous as the Reynolds number increases, with a reversal in their relative performance occurring around Re = 200. This behaviour can be interpreted in terms of the different flow redistribution mechanisms induced by the two geometries. Although the rectangular and triangular ribs have the same frontal-area blockage ratio, the rectangular ribs produce a more uniform obstruction along the channel height, whereas the triangular ribs induce a vertically non-uniform redistribution of the flow, as illustrated in Figures 9 and 10. As Reynolds number increases, inertial effects become progressively more important, modifying the relative effectiveness of these mechanisms and favouring the heat-transfer enhancement associated with the triangular geometry at higher Reynolds numbers. This Reynolds-number-dependent change in ranking is consistent with previous observations that the relative performance of different rib profiles depends strongly on the operating conditions and cannot be established from rib shape alone [29–31].

The enhancement in heat transfer is accompanied by an increase in hydraulic resistance. As shown in Figure 11d, the Fanning friction factor of both ribbed configurations remains substantially higher than that of the smooth channel. At Re = 400, f is approximately 0.040 for the smooth configuration and about 0.092 and 0.100 for the rectangular and h4w2s1 configurations, respectively. This behaviour results from the combined effects of flow constriction, acceleration around the ribs, separation, recirculation, and form drag. Similar thermal–hydraulic trade-offs have been reported for triangular and other rib geometries in microchannels [29,30,33,34]. The combined effect of heat-transfer enhancement and hydraulic penalty is summarized by the PEC in Figure 11e. At the lowest Reynolds numbers, both ribbed configurations provide PEC values close to or below unity, indicating that the heat-transfer enhancement is not yet sufficient to compensate for the associated increase

in flow resistance according to the adopted performance criterion. The rectangular rib performs slightly better in this range. As Reynolds number increases, however, the stronger increase in Nusselt number produced by the triangular rib progressively compensates for its somewhat higher friction factor. The two configurations exhibit comparable performance around Re = 200, after which h4w2s1 becomes superior. At Re = 400, PEC reaches 1.71 for the triangular configuration compared with 1.57 for the rectangular one, corresponding to an improvement of 8.7%. The complementary indicators based on the externally heated surface, shown in Figure 11c,f, confirm the general trends observed for the conventional Nusselt number and PEC. In particular, both Nu_h and PEC_h reproduce the Reynolds-number-dependent change in the relative performance of the rectangular and triangular ribs, with h4w2s1 becoming more advantageous at higher Reynolds numbers. This agreement indicates that the improved performance of the triangular configuration is also retained when the cooling effectiveness is evaluated with reference to the heated base.

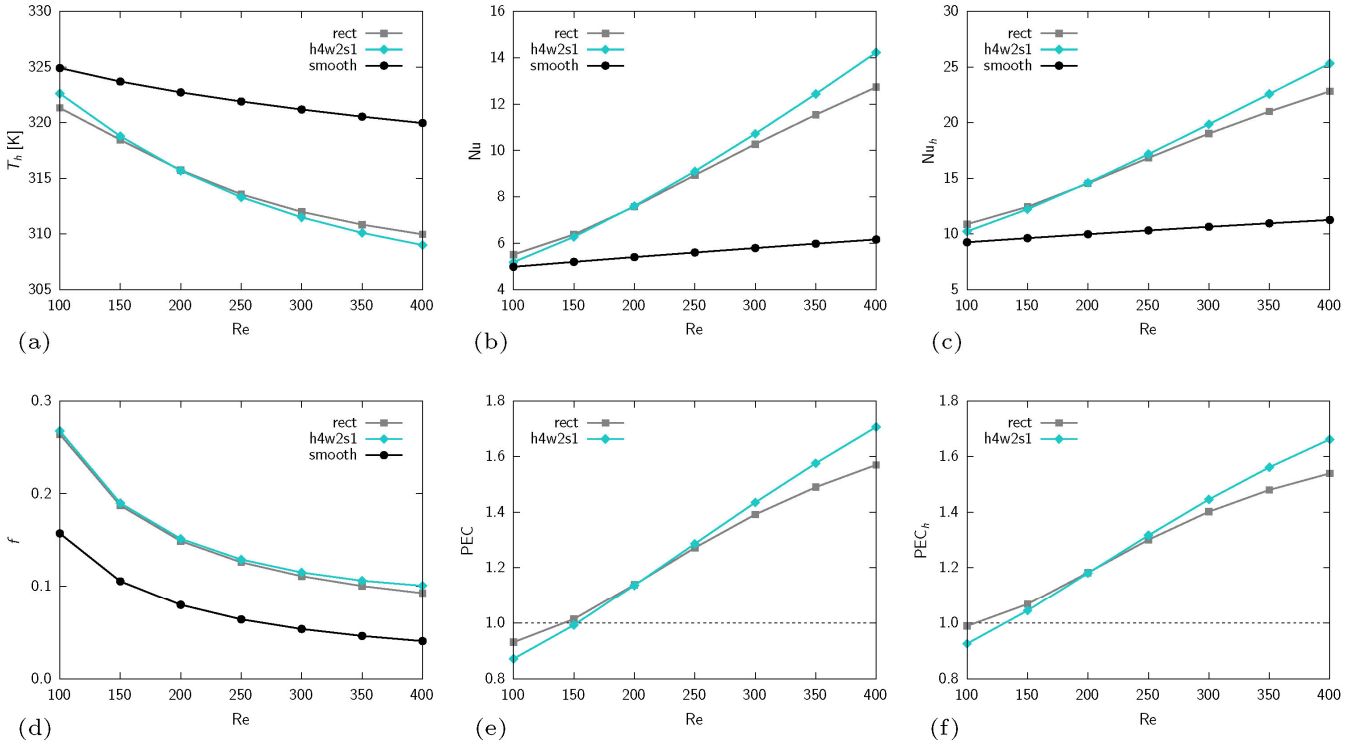


Figure 11. Quantitative comparison of the smooth, rectangular, and h4w2s1 MCHS configurations at different Reynolds numbers in terms of: average heated-wall temperature (**a**), Nusselt number (**b**), overall Nusselt number (**c**), Fanning friction factor (**d**), PEC (**e**), and PEC_h (**f**).

These results show that maintaining the same frontal-area blockage ratio does not lead to equivalent thermohydraulic behaviour. The manner in which the obstruction is geometrically distributed within the channel cross-section substantially affects the induced flow structures and their interaction with the thermal field. On the basis of this comparison, the transverse-section triangular rib was retained for the subsequent parametric investigation of rib width, height, and spacing.

4.2. Effect of Triangular-Rib Width on Thermohydraulic Performance

Following the rib-shape comparison, the influence of triangular-rib width was investigated by considering configurations h4w1s1, h4w2s1, and h4w3s1. In this series, the rib height is maintained equal to the full channel height, $h = H_{ch} = 0.20$ mm, and the spacing is

fixed at $s = 0.20$ mm, while the rib width is increased from 0.025 to 0.075 mm. Consequently, the frontal-area blockage ratio increases from 12.5% to 37.5%.

Since the fundamental flow and heat-transfer mechanisms associated with triangular ribs were clarified in the previous section, the parametric investigations of rib width, height, and spacing in the following subsections prioritize quantitative performance analysis. Accordingly, the results are first discussed in terms of average heated-wall temperature, Nu, f, and PEC, followed by selected qualitative fields to elucidate the physical origins of the observed trends. Figure 12 summarizes the corresponding thermal and hydraulic performance. Increasing rib width produces a marked reduction in the average heated-wall temperature, particularly at the higher Reynolds numbers. At Re = 400, the wall temperature decreases from approximately 317 K for h4w1s1 to about 309 K for h4w2s1 and approximately 305 K for h4w3s1.

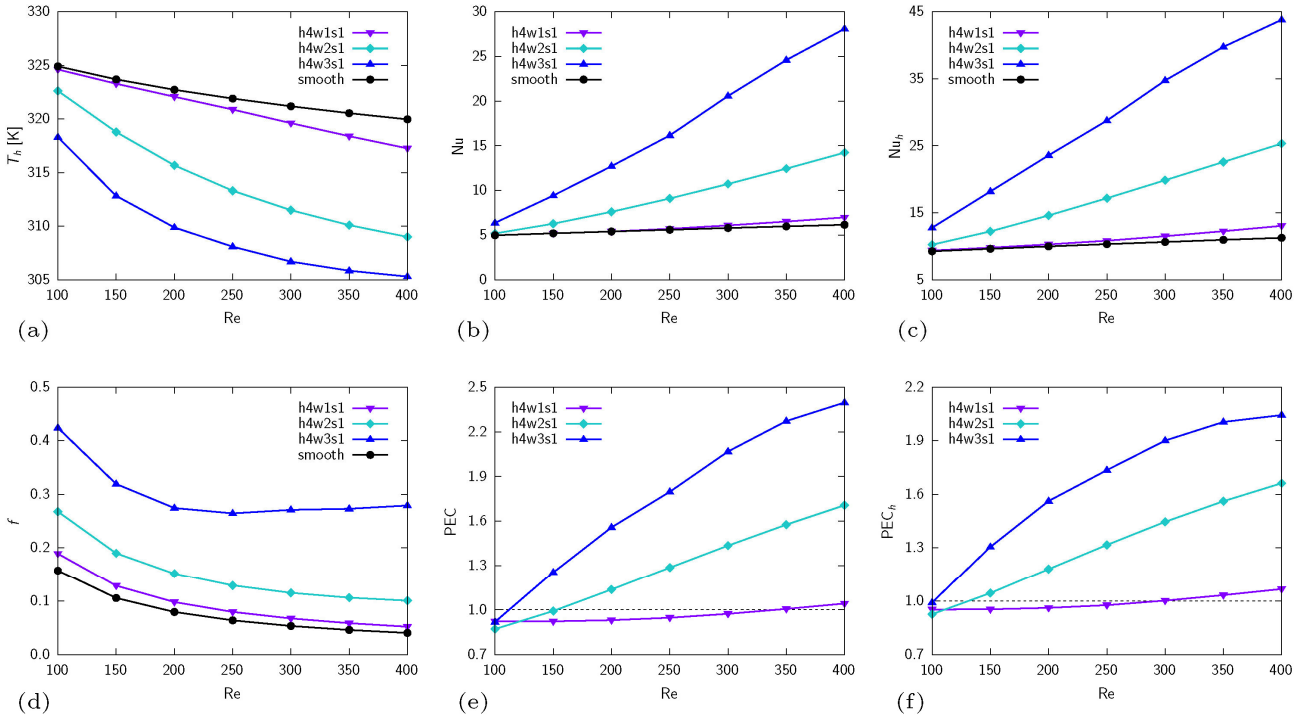


Figure 12. Quantitative comparison of the smooth, h4w1s1, h4w2s1 and h4w3s1 MCHS configurations at different Reynolds numbers in terms of: average heated-wall temperature (**a**), Nusselt number (**b**), overall Nusselt number (**c**), Fanning friction factor (**d**), PEC (**e**), and PEC_h (**f**).

The effect of rib width therefore becomes progressively more pronounced as the Reynolds number increases. This trend is reflected in the conventional Nusselt number (Figure 12b). At Re = 400, Nu increases from 6.97 for h4w1s1 to 14.23 for h4w2s1 and 28.10 for h4w3s1. Thus, tripling the rib width from 0.025 to 0.075 mm produces an approximately fourfold increase in Nusselt number within the investigated range. This enhancement cannot be attributed solely to the increase in heat-transfer surface area. Indeed, at Re = 400, the h4w3s1 configuration exhibits a fluid–solid interfacial area per unit channel length only 10.6% larger than that of the smooth microchannel, whereas its conventional Nusselt number is approximately 356% higher. The complementary overall Nusselt number Nu_h (Figure 12c), defined with reference to the fixed heated-base area, exhibits a similar dependence on rib width and Reynolds number. From a fluid-dynamic perspective, increasing rib width causes a progressively larger fraction of the channel cross-section to be intercepted by the obstruction, producing stronger flow deflection, local acceleration, separation, and redistribution of momentum within the channel. Despite the substantial increase in hy-

draulic resistance (Figure 12d), the PEC (Figure 12e) improves with rib width, particularly at higher Reynolds numbers. At Re = 400, PEC increases from 1.04 for h4w1s1 to 1.71 for h4w2s1 and 2.40 for h4w3s1. The complementary PEC_h (Figure 12f) exhibits a similar trend, with the thermohydraulic advantage of wider ribs becoming progressively more pronounced as Reynolds number increases. Therefore, both performance criteria indicate that the additional heat-transfer enhancement outweighs the associated hydraulic penalty at higher Reynolds numbers. Within the investigated range, h4w3s1 provides the highest overall thermohydraulic performance and is consequently retained for the subsequent spacing investigation.

The velocity and thermal fields shown in Figures 10, 13 and 14 support this interpretation. The narrow h4w1s1 rib produces relatively limited disturbance of the main flow, whereas increasing the width progressively enlarges the region affected by the rib and strengthens the downstream separated flow. The local cooling patterns associated with fluid impingement on the inclined triangular-rib surfaces become more pronounced as rib width increases, as illustrated by the comparison between Figures 13b and 14b. In particular, the narrower ribs of h4w1s1 induce weaker flow deflection, making these low-temperature regions less evident. The h4w3s1 configuration consequently exhibits the strongest modification of the near-rib flow field and the lowest wall-temperature levels. Similar qualitative trends have been reported in previous investigations in which increasing triangular-rib dimensions enhanced heat transfer by intensifying flow disturbance and boundary-layer redevelopment [32,34,36].

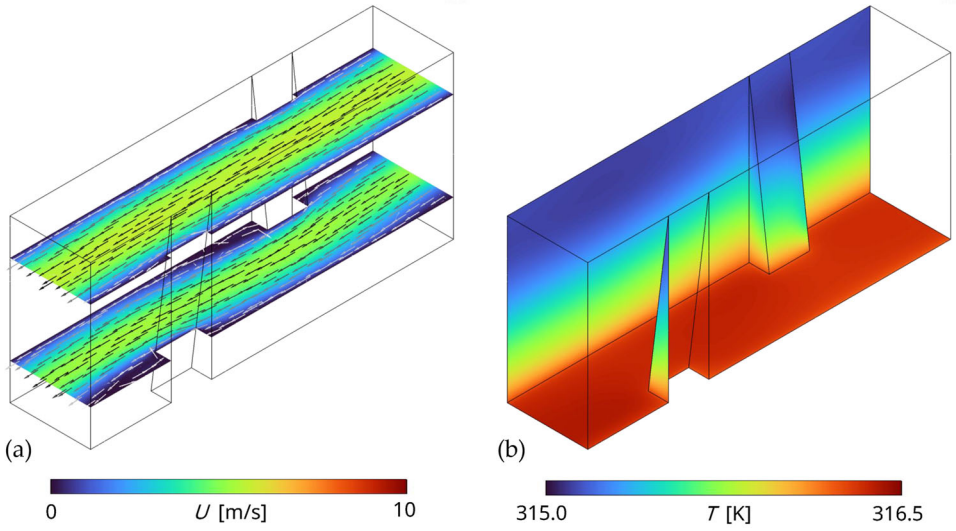


Figure 13. Velocity and temperature fields for the h4w1s1 MCHS at Re = 400: velocity-magnitude contours with velocity vectors (**a**); temperature distribution on the microchannel walls (**b**).

The thermal improvement is accompanied by a considerable hydraulic penalty. As shown in Figure 12d, at Re = 400 the Fanning friction factor increases from 0.052 for h4w1s1 to 0.100 for h4w2s1 and 0.279 for h4w3s1. The increase becomes particularly pronounced for the widest rib, indicating that form drag and losses associated with flow separation become increasingly important as the blockage ratio increases.

Unlike h4w1s1 and h4w2s1, for which the friction factor decreases monotonically with Reynolds number, h4w3s1 exhibits a minimum at approximately Re = 250, followed by a slight increase at higher Reynolds numbers. This departure from the general trend is associated with the flow structures shown in Figure 15, which presents the velocity vectors on the plane $z = 0.22H_{ch}$ for h4w2s1 and h4w3s1 at different Reynolds numbers. Velocity vectors are displayed with uniform length, regardless of their magnitude, to highlight the

local flow structures. For h4w2s1, the recirculation region downstream of the ribs progressively enlarges as the Reynolds number increases, indicating increasingly pronounced flow disturbance. In contrast, for h4w3s1, the recirculation zone increases in size from Re = 100 to 250 and subsequently decreases as the Reynolds number rises from 250 to 400. This reorganization of the downstream recirculation pattern is consistent with the observed change in friction-factor behaviour, since variations in flow separation and reattachment can alter the overall hydraulic resistance at higher Reynolds numbers. To investigate this behaviour more quantitatively, the three-dimensional flow fields of configurations h4w2s1 and h4w3s1 were analyzed using two complementary parameters characterizing the regions of reverse axial flow. Previous numerical investigations have quantified the extent of reverse flow by identifying regions characterized by a negative streamwise velocity component and evaluating their volume relative to that of the fluid domain [48,49]. Following a similar approach, the reverse flow volume fraction R_{rev} is defined as the percentage of the total fluid volume in which the streamwise velocity component is negative. To complement this geometrical measure, a reverse flow intensity index I_{rev} is introduced in the present study. This parameter represents the percentage contribution of these regions to the volume integral of the absolute streamwise velocity component over the entire fluid domain. The two parameters are defined as follows:

$$R_{rev} = \frac{100}{\Omega}\int_{\Omega} \mathcal{H}(-u_a)\, d\Omega \tag{14}$$

$$I_{rev} = 100\,\frac{\int_{\Omega} \mathcal{H}(-u_a)|u_a|\, d\Omega}{\int_{\Omega} |u_a|\, d\Omega} \tag{15}$$

respectively, where Ω is the total fluid volume, u_a is the streamwise velocity component, and $\mathcal{H}(-u_a)$ is equal to unity for $u_a < 0$ and zero otherwise. While R_{rev} quantifies the spatial extent of reverse axial flow, I_{rev} additionally accounts for its relative intensity.

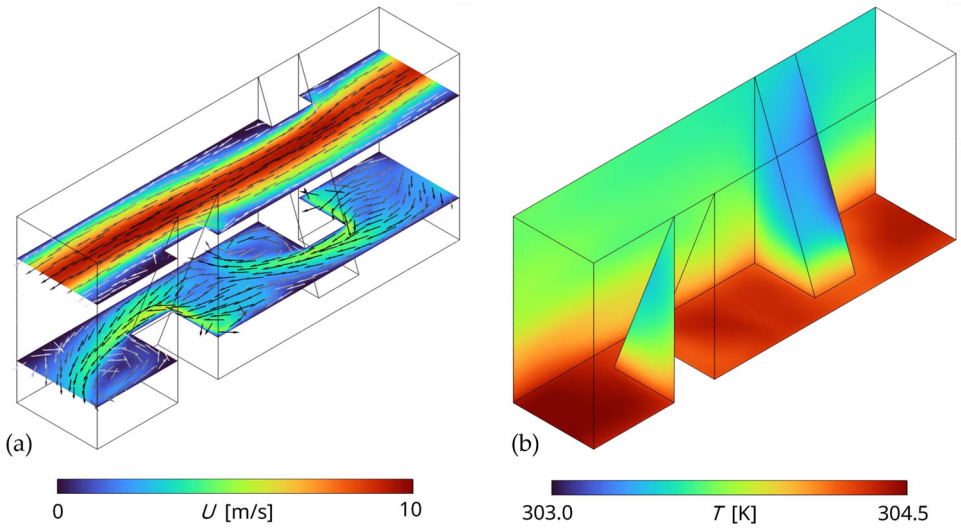


Figure 14. Velocity and temperature fields for the h4w3s1 MCHS at Re = 400: velocity-magnitude contours with velocity vectors (**a**); temperature distribution on the microchannel walls (**b**).

The results reported in Table 3 reveal markedly different flow behaviours for the two configurations. For h4w2s1, both reverse flow indicators increase monotonically with Reynolds number, while over the same Reynolds number range the Fanning friction factor decreases continuously. In contrast, h4w3s1 exhibits a non-monotonic variation in the reverse flow volume fraction, which increases from 11.76% at Re = 100 to a maximum of 14.13% at Re = 200 and then generally decreases, reaching 12.59% at Re = 400. Conversely, the reverse flow intensity index increases continuously throughout the investigated

Reynolds number range, from 0.60% to 2.29%. In particular, between Re = 250 and Re = 400, the reverse flow volume fraction of h4w3s1 decreases by approximately 8.7%, while its intensity index increases by approximately 47%, which means that the reduction in the spatial extent of reverse axial flow is accompanied by an increase in its relative intensity. Over the same interval, the Fanning friction factor increases from 0.26449 to 0.27909, corresponding to an increase of approximately 5.5%.

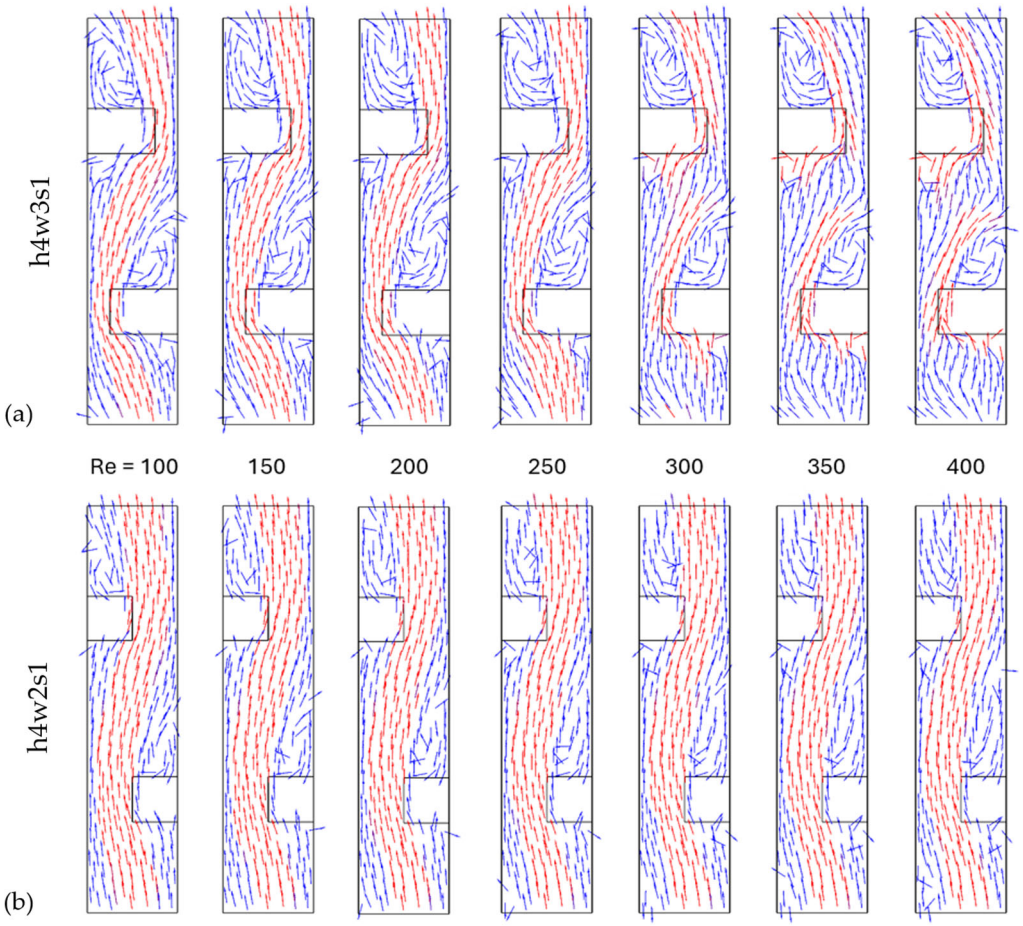


Figure 15. Velocity vector fields at different Reynolds numbers for h4w3s1 (**a**) and h4w2s1 (**b**) configurations. Velocity vectors are displayed with uniform length on a sectional plane above the channel base located at z = 0.22 H_{ch}, while the triangular rib outlines represent the projections of the ribs onto the channel base plane. Red and blue vectors indicate regions of relatively higher and lower velocity magnitude, respectively.

Table 3. Fanning friction factor, reverse flow volume fraction, and reverse flow intensity index for configurations h4w2s1 and h4w3s1 at different Reynolds numbers.

Configuration	Parameter	Re = 100	150	200	250	300	350	400
h4w2s1	f [−]	0.2677	0.1898	0.1512	0.1288	0.1148	0.1059	0.1004
	R_{rev} [%]	4.04	5.47	6.48	7.28	7.95	8.57	9.17
	I_{rev} [%]	0.11	0.20	0.29	0.36	0.44	0.51	0.59
h4w3s1	f [−]	0.4241	0.3192	0.2744	0.2645	0.2709	0.2731	0.2791
	R_{rev} [%]	11.76	13.59	14.13	13.80	12.68	12.39	12.59
	I_{rev} [%]	0.60	0.96	1.22	1.55	1.84	2.04	2.29

This behaviour quantitatively confirms the Reynolds-number-dependent reorganization of the separated flow structures suggested by the velocity vector fields in Figure 15.

These findings provide quantitative evidence that the non-monotonic friction-factor behaviour of h4w3s1 is accompanied by a redistribution of the three-dimensional reverse flow regions, involving changes in both their extent and relative intensity.

4.3. Effect of Triangular-Rib Height on Thermohydraulic Performance

The second geometric parameter investigated is rib height. Configurations h1w4s1, h2w4s1, and h3w4s1 have the same full rib width, $w = W_{ch} = 0.10$ mm, and the same spacing $s = 0.20$ mm, while the rib height is increased from 0.05 to 0.15 mm. The corresponding frontal-area blockage ratios are 12.5%, 25%, and 37.5%, respectively.

Figure 16 shows that increasing rib height progressively improves heat removal from the heated base. The average wall temperature decreases with increasing Reynolds number for all cases and, at a given Reynolds number, decreases systematically as the rib height increases. At Re = 400, the average heated-wall temperature is approximately 314 K for h1w4s1, 310 K for h2w4s1, and 307 K for h3w4s1, compared with approximately 320 K for the smooth reference. The corresponding Nusselt-number results show the same systematic dependence on rib height. At Re = 400, Nu increases from 8.59 for h1w4s1 to 11.91 for h2w4s1 and 18.09 for h3w4s1. Increasing the rib height therefore produces a progressively stronger enhancement of convection. The alternative indicators Nu_h and PEC_h exhibit trends broadly consistent with those of the conventional performance parameters. While Nu_h increases systematically with rib height, PEC_h highlights the stronger relative hydraulic penalty associated with taller ribs at the lowest Reynolds numbers. As Reynolds number increases, the additional thermal enhancement becomes progressively more effective in compensating for this penalty, and h3w4s1 provides the highest PEC_h values among the configurations with variable rib height.

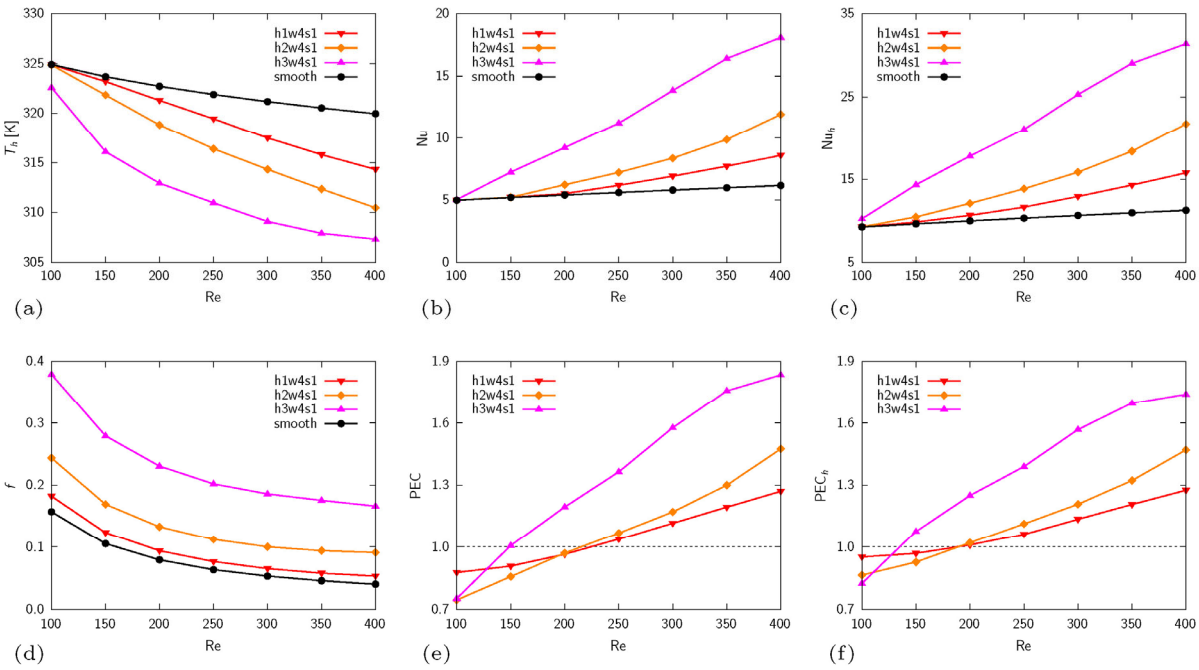


Figure 16. Quantitative comparison of the smooth, h1w4s1, h2w4s1 and h3w4s1 MCHS configurations at different Reynolds numbers in terms of: average heated-wall temperature (**a**), Nusselt number (**b**), overall Nusselt number (**c**), Fanning friction factor (**d**), PEC (**e**), and PEC_h (**f**).

The velocity fields shown in Figures 17–19 indicate that taller ribs disturb a larger portion of the channel cross-section and produce more pronounced separated and recirculating regions. This strengthens momentum exchange between different portions of the flow

and periodically perturbs the thermal boundary layer. Localized low-temperature regions can also be observed on the inclined rib surfaces in Figures 17b, 18b and 19b, indicating that the local cooling mechanism associated with flow impingement is also present in the configurations with variable rib height. The extent and intensity of these regions vary with rib height, reflecting differences in the local flow deflection and fluid-surface interaction.

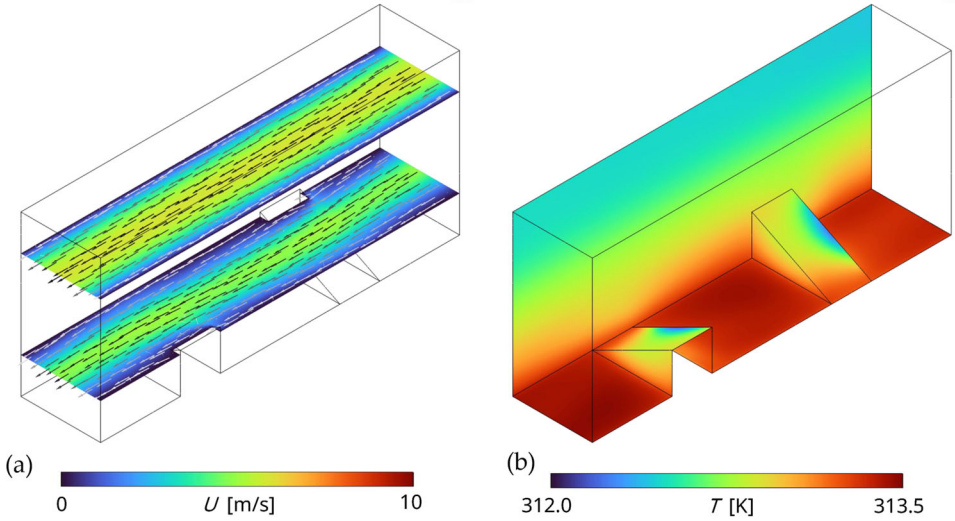


Figure 17. Velocity and temperature fields for the h1w4s1 MCHS at Re = 400: velocity-magnitude contours with velocity vectors (**a**); temperature distribution on the microchannel walls (**b**).

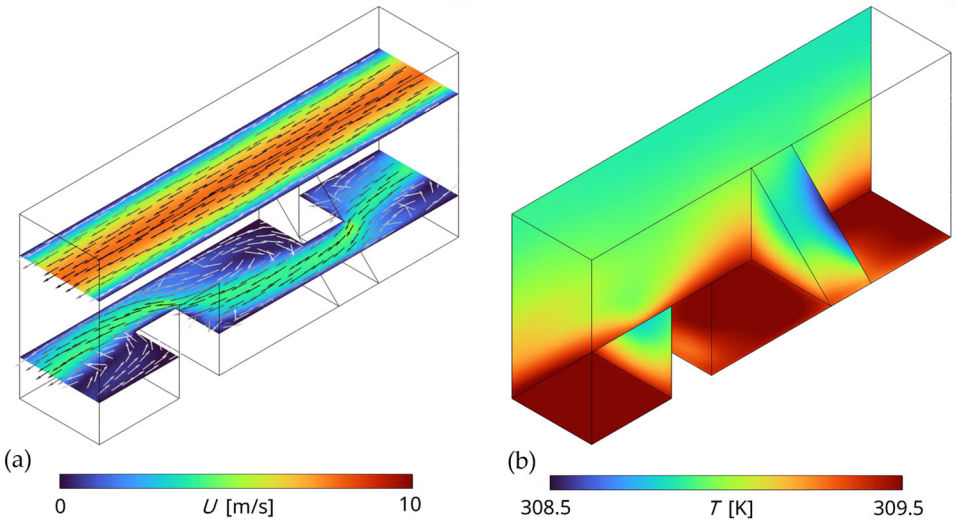


Figure 18. Velocity and temperature fields for the h2w4s1 MCHS at Re = 400: velocity-magnitude contours with velocity vectors (**a**); temperature distribution on the microchannel walls (**b**).

The effect of rib height on heat transfer is qualitatively consistent with the findings of Feng et al. [36], who reported increasing heat-transfer enhancement with increasing height of partial-height triangular ribs, and with the broader trends reported for periodic triangular-rib arrangements [38].

The improvement in thermal performance is accompanied by higher hydraulic resistance. At Re = 400, the Fanning friction factor increases from 0.054 for h1w4s1 to 0.091 for h2w4s1 and 0.166 for h3w4s1. Increasing rib height therefore increases both the fraction of the cross-section affected by the obstruction and the associated form drag and separation losses. The PEC results show, however, that the thermal enhancement remains sufficiently large to compensate for the additional hydraulic penalty over most of the investigated Reynolds-number range.

At Re = 400, PEC increases from 1.27 for h1w4s1 to 1.48 for h2w4s1 and 1.83 for h3w4s1. The advantage of increasing rib height is therefore evident not only from the heat-transfer coefficient but also from the combined thermohydraulic criterion.

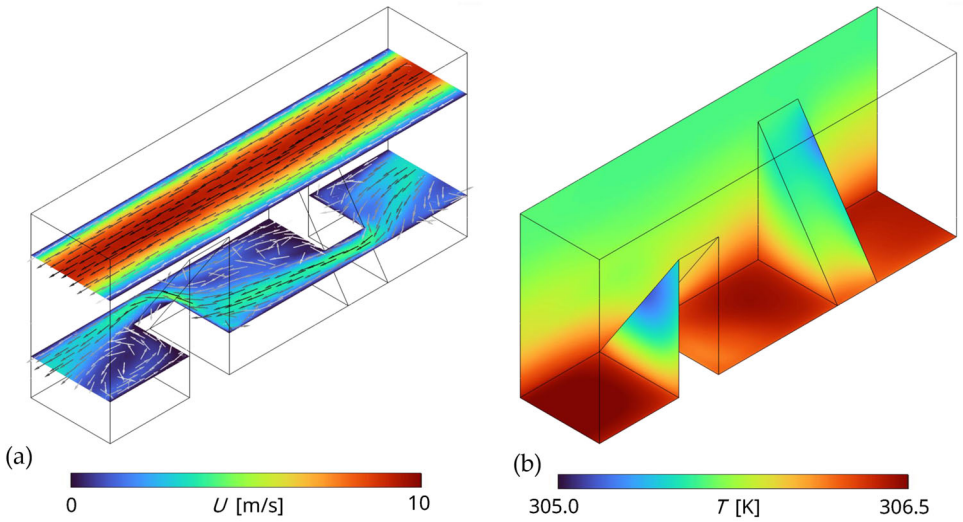


Figure 19. Velocity and temperature fields for the h3w4s1 MCHS at Re = 400: velocity-magnitude contours with velocity vectors (**a**); temperature distribution on the microchannel walls (**b**).

These results demonstrate that rib height is an effective parameter for strengthening the interaction between the obstruction and the channel flow. Nevertheless, comparison with the rib-width series also indicates that configurations having the same blockage ratio do not necessarily provide equivalent performance. This aspect is examined explicitly in the following subsection.

4.4. Comparison of Triangular Ribs at Matched-Blockage Ratios

The preceding analyses considered the effects of rib width and height separately. However, because the triangular frontal area is proportional to the product $h \cdot w$, the two geometric series also contain configurations having identical frontal-area blockage ratios BR but markedly different aspect ratios. Three matched-blockage pairs can be identified: h4w1s1 and h1w4s1 at BR = 12.5%, h4w2s1 and h2w4s1 at BR = 25%, and h4w3s1 and h3w4s1 at BR = 37.5%. Within each pair, one configuration distributes the obstruction predominantly along the channel height (full-height/variable-width family), whereas the other distributes it predominantly along the channel width (full-width/variable-height family). Rib spacing is identical for all these comparisons.

The results clearly demonstrate that equal blockage ratio does not imply equal thermohydraulic behaviour. Moreover, the effect of blockage distribution changes with the blockage level. At BR = 12.5%, the full-width/low-height configuration h1w4s1 provides a higher Nusselt number and PEC than the corresponding full-height/narrow configuration h4w1s1. From Figures 12 and 16, at Re = 400, Nu is 8.59 for h1w4s1 compared with 6.97 for h4w1s1, while the corresponding PEC values are 1.27 and 1.04. Thus, at relatively low blockage, distributing the triangular obstruction over a larger fraction of the channel width appears more effective than extending a narrow obstruction over the full channel height. The relative behaviour changes at BR = 25%. The full-height configuration h4w2s1 produces a Nusselt number of 14.23 at Re = 400, compared with 11.91 for h2w4s1, while the corresponding PEC values are 1.71 and 1.48. The full-height/variable-width arrangement therefore becomes thermohydraulically advantageous at this intermediate blockage level. The distinction becomes considerably more pronounced at BR = 37.5%. At Re = 400, h4w3s1 reaches a Nusselt number of 28.10 and a PEC of 2.40, whereas the

corresponding h3w4s1 configuration reaches Nu = 18.09 and PEC = 1.83. At the highest blockage ratio, this corresponds to increases of 55.3% in Nusselt number and 30.7% in PEC for the full-height/variable-width configuration. The full-height configuration also exhibits a substantially larger friction factor, indicating stronger flow obstruction and form drag; nevertheless, the additional heat-transfer enhancement is sufficiently large to produce a higher PEC.

These comparisons indicate that the frontal-area blockage ratio alone is insufficient to characterize the performance of the present triangular ribs. At a fixed value of BR, changing the rib aspect ratio modifies how the obstruction interacts with different regions of the channel cross-section, thereby altering flow acceleration, separation and reattachment, recirculation, and thermal-boundary-layer redevelopment. The balance among these mechanisms depends on the blockage level itself, as demonstrated by the change in ranking between the BR = 12.5% pair and the higher-blockage configurations. Previous microchannel studies have independently demonstrated strong effects of triangular-rib width, height, protrusion, and orientation on heat transfer and pressure loss [32,34,36–38]. However, within the literature reviewed in the present work, an equivalent systematic comparison between full-height/variable-width and full-width/variable-height transverse-section triangular ribs at matched frontal-area blockage ratios was not identified. The present comparison therefore highlights a distinct design consideration: not only the amount of frontal blockage, but also its spatial distribution within the channel cross-section, must be considered when assessing rib-induced thermohydraulic enhancement.

4.5. Effect of Triangular-Rib Spacing on Thermohydraulic Performance

Based on the preceding parametric analysis, h4w3s1 exhibited the highest PEC among the investigated width and height configurations and was therefore selected to examine the effect of rib spacing. Configurations h4w3s1, h4w3s2, and h4w3s3 have identical rib height and width, corresponding to BR = 37.5%, while the streamwise spacing is increased from 0.20 to 0.40 mm. This comparison therefore allows the effect of rib spacing to be assessed while maintaining the same frontal obstruction for each individual rib, although both the disturbance frequency and the fluid–solid interfacial area per unit channel length vary.

Figure 20 shows that reducing rib spacing strongly improves thermal performance. At Re = 400, the average heated-wall temperature decreases from around 311 K for s = 0.40 mm to about 307 K for s = 0.30 mm and approximately 305 K for s = 0.20 mm. Consistently, the Nusselt number increases from 12.07 for h4w3s3 to 19.66 for h4w3s2 and 28.10 for h4w3s1. This behaviour results from the combined effects of the increased fluid–solid interfacial area per unit channel length and the modifications of the flow field associated with more closely spaced ribs. In particular, reducing rib spacing increases the frequency of flow disturbance, as the flow encounters a new obstruction before the velocity and thermal boundary layers can substantially redevelop toward their undisturbed state.

The variation in the available heat-transfer area can also be quantified by considering the fluid–solid interfacial area per unit channel length. Reducing rib spacing from 0.40 to 0.20 mm increases this area by approximately 4.7%, whereas the conventional Nusselt number increases by 132.8% at Re = 400. This comparison further indicates that the observed enhancement cannot be explained solely by the increase in interfacial area, but also reflects the modified convective heat-transfer conditions associated with more closely spaced ribs. The complementary indicators Nu_h and PEC_h confirm the beneficial effect of reducing rib spacing. Both parameters increase as the ribs are placed closer together, with h4w3s1 providing the highest PEC_h throughout the investigated Reynolds number range. Thus, the thermohydraulic advantage associated with smaller rib spacing is also confirmed when the thermal performance is evaluated with reference to the externally heated surface.

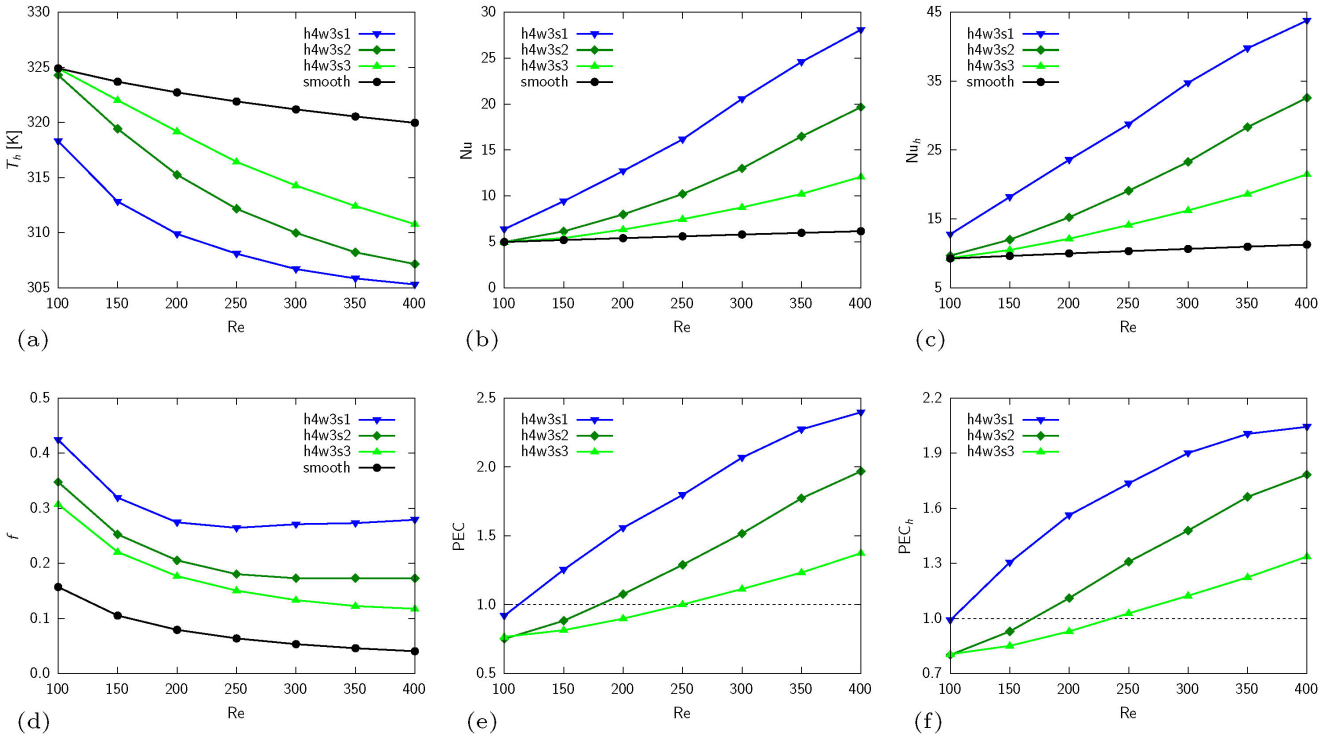


Figure 20. Quantitative comparison of the smooth, h4w3s1, h4w3s2 and h4w3s3 MCHS configurations at different Reynolds numbers in terms of: average heated-wall temperature (**a**), Nusselt number (**b**), overall Nusselt number (**c**), Fanning friction factor (**d**), PEC (**e**), and PEC_h (**f**).

The velocity and temperature fields in Figures 14, 21 and 22 are consistent with this interpretation: h4w3s1 exhibits the strongest disturbance and lowest wall-temperature levels, whereas the longer-spacing configurations allow a greater degree of flow and thermal recovery between successive ribs. The increased disturbance frequency also produces a significant pressure-loss penalty. At Re = 400, the Fanning friction factor increases from 0.118 for $s = 0.40$ mm to 0.173 for $s = 0.30$ mm and 0.279 for $s = 0.20$ mm. Thus, reducing the spacing by 50% increases the Fanning friction factor by approximately 137%. For h4w3s2 and h4w3s3, f decreases monotonically with Reynolds number, whereas h4w3s1 retains the non-monotonic high-Reynolds-number behaviour discussed in Section 4.2. Despite the higher hydraulic penalty, the PEC increases substantially as rib spacing decreases. At Re = 400, PEC rises from 1.37 for h4w3s3 to 1.97 for h4w3s2 and 2.40 for h4w3s1. Reducing the spacing from 0.40 to 0.20 mm therefore increases PEC by 74.5%, demonstrating that, within the investigated range, the additional heat-transfer enhancement more than compensates for the associated increase in pressure losses.

This trend agrees qualitatively with the results of Alnaimat et al. [37], who found that reducing the pitch of triangular sidewall ribs decreases thermal resistance but increases pumping requirements. Chai et al. [34] likewise identified rib spacing as an important parameter controlling both heat-transfer augmentation and frictional losses. Although the geometrical orientation of the ribs in those studies differs from the present transverse-section configuration, the underlying trade-off between more frequent boundary-layer disruption and increased hydraulic resistance is consistent.

The present results therefore indicate that rib spacing provides an additional degree of control over the thermohydraulic performance after rib cross-sectional geometry has been selected. Within the range $0.2 \leq s \leq 0.4$ mm, the smallest investigated spacing provides the highest PEC and PEC_h.

It should be noted that h4w3s1 provides the highest values of both PEC and PEC_h among the investigated configurations. However, since the analysis is limited to selected rib dimensions and spacings, this result does not necessarily represent a global optimum.

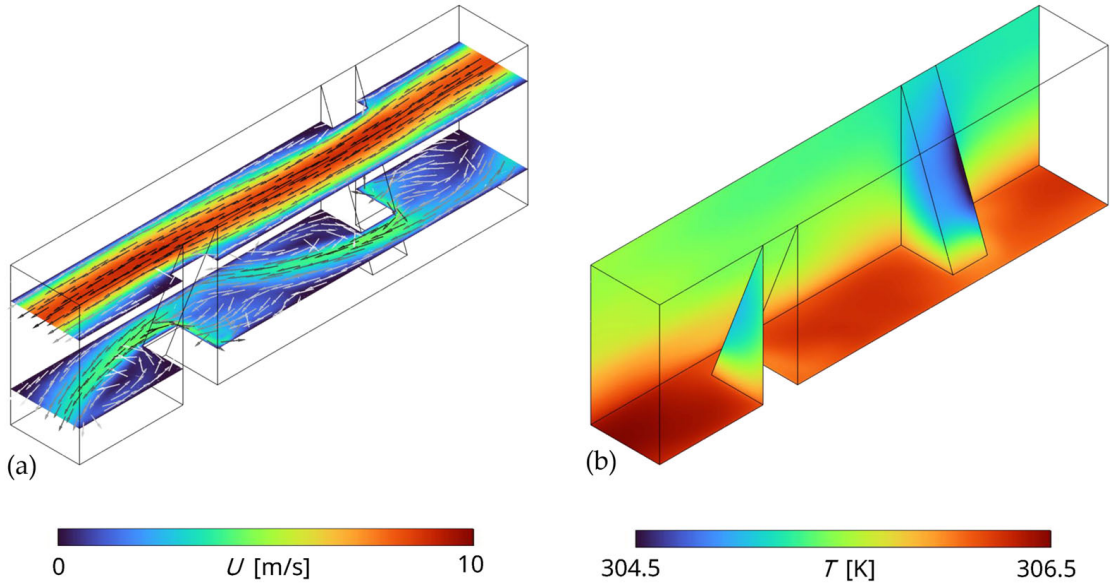


Figure 21. Velocity and temperature fields for the h4w3s2 MCHS at Re = 400: velocity-magnitude contours with velocity vectors (**a**); temperature distribution on the microchannel walls (**b**).

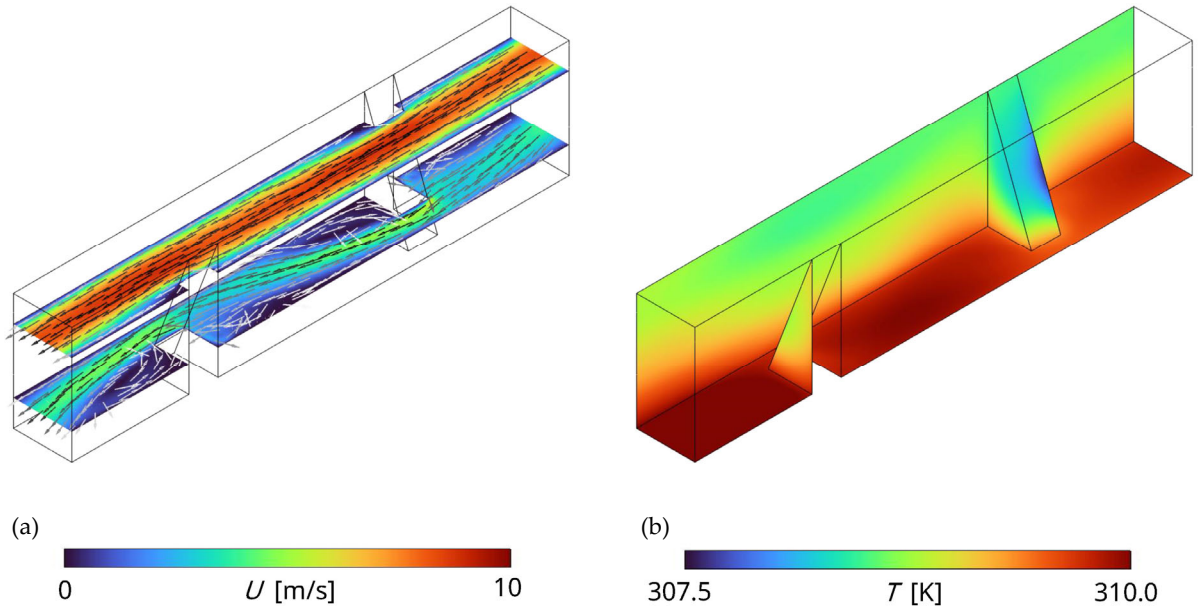


Figure 22. Velocity and temperature fields for the h4w3s3 MCHS at Re = 400: velocity-magnitude contours with velocity vectors (**a**); temperature distribution on the microchannel walls (**b**).

4.6. Additional Thermohydraulic Performance Indicators

To complement the preceding parametric analyses, this section provides an overall assessment of the investigated configurations from two additional perspectives. Field-synergy analysis is used to further investigate the relationship between flow and heat transfer, while a direct comparison of pressure drops provides a quantitative evaluation of the hydraulic penalties associated with the different rib geometries.

Figure 23 shows the relationship between the cosine of the global effective synergy angle β_m defined by Equation (12) and the heat-transfer enhancement ratios obtained using

the conventional Nu/Nu_0 and alternative $Nu_h/Nu_{h,0}$ Nusselt-number definitions. An overall inverse relationship can be observed, with smaller synergy angles (larger cosines) generally associated with higher Nusselt-number enhancement ratios. This trend is consistent with the effects of rib geometry discussed in Sections 4.1–4.5: increasing rib width or height, as well as reducing rib spacing, generally leads to smaller synergy angles and higher heat-transfer enhancement. The h4w3s1 configuration exhibits the lowest synergy angles and the highest Nusselt number ratios among the investigated geometries. Moreover, within each configuration, increasing the Reynolds number generally results in smaller synergy angles and higher enhancement ratios. These observations indicate that the global effective synergy angle correlates well with the thermal performance trends associated with both rib geometry and Reynolds number.

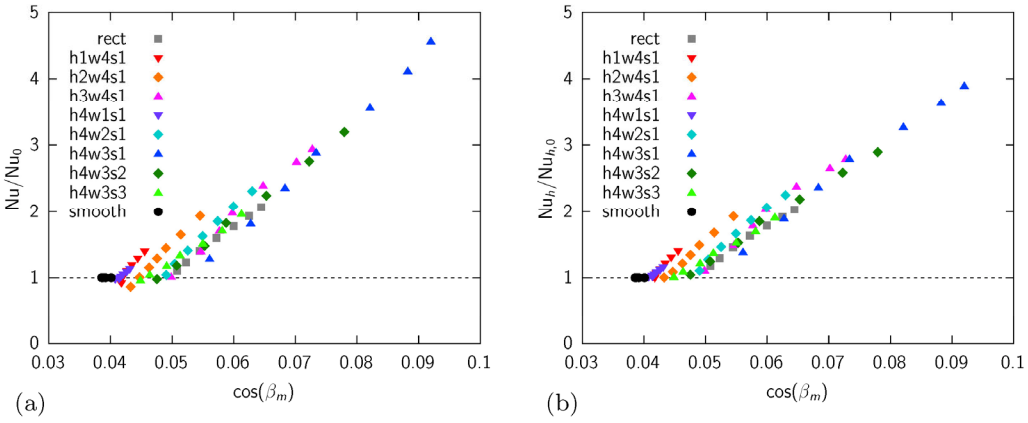


Figure 23. Relationship between the cosine of the global effective synergy angle and the Nusselt-number enhancement ratios for the investigated ribbed-microchannel configurations: (**a**) Nu/Nu_0; (**b**) $Nu_h/Nu_{h,0}$.

An important difference emerges between the two panels. When the conventional Nusselt number is considered (see Figure 23a), some ribbed configurations exhibit enhancement ratios below unity, despite the additional heat-transfer surfaces. This behaviour arises from the dependence of the conventional heat-transfer coefficient on the actual fluid–solid interfacial area. Consequently, a lower conventional Nusselt number does not necessarily indicate poorer overall cooling effectiveness. In contrast, all investigated ribbed configurations exhibit enhancement ratios greater than unity when the alternative Nusselt number based on the externally heated surface is considered; see Figure 23b, highlighting the usefulness of this complementary performance indicator.

The range of cosine values pertaining to the points shown in the graphs of Figure 23 corresponds to relatively high synergy angles, approximately between 84.7° and 87.8°. This can be attributed to the global nature of β_m, since the integration over the entire fluid domain accounts for regions characterized by different degrees of alignment between the velocity and temperature-gradient fields, including regions contributing less effectively to convective heat transfer. Consequently, localized improvements in field synergy may produce only limited changes in the global angle, even when they are associated with substantial heat-transfer enhancement.

To complement the analysis based on the Fanning friction factor, Table 4 reports the pressure drops for all investigated configurations at Re = 100 and Re = 400, referred to an equivalent channel length of 10 mm. The corresponding ratios relative to the smooth microchannel are also provided to facilitate comparison among the different geometries.

Table 4. Pressure drop over 10 mm and pressure-drop ratio relative to the smooth channel at Re = 100 and 400.

Configuration	Δp [kPa]		$\Delta p/\Delta p_0$	
	Re = 100	**Re = 400**	**Re = 100**	**Re = 400**
smooth	13.36	55.08	1.00	1.00
rect	22.45	125.68	1.68	2.28
h4w1s1	16.07	70.84	1.20	1.29
h4w2s1	22.76	136.61	1.70	2.48
h4w3s1	36.06	379.72	2.70	6.89
h1w4s1	15.49	72.92	1.16	1.32
h2w4s1	20.72	124.14	1.55	2.25
h3w4s1	32.22	226.26	2.41	4.11
h4w3s2	29.56	235.04	2.21	4.27
h4w3s3	26.13	159.89	1.96	2.90

The results are consistent with the trends previously observed for the friction factor, confirming that the introduction of ribs leads to substantial increases in hydraulic resistance, which become particularly pronounced for configurations with larger blockage ratios and smaller rib spacings. At Re = 400, the pressure drop increases from 55.08 kPa for the smooth microchannel to 379.72 kPa for h4w3s1, corresponding to an increase by a factor of approximately 6.89. A comparison between the rectangular and triangular configurations at the same blockage ratio of 25% shows relatively similar pressure losses, with values of 125.68 and 136.61 kPa, respectively.

The influence of rib spacing is also particularly significant. For the h4w3s* configurations, increasing the spacing from 0.20 to 0.40 mm reduces the pressure drop from 379.72 to 159.89 kPa at Re = 400, corresponding to a reduction of approximately 58%. Furthermore, the pressure-drop ratios relative to the smooth microchannel generally increase with Reynolds number, indicating that the hydraulic penalty associated with the ribs becomes progressively more severe at higher flow rates, particularly for the most obstructive configurations.

These results highlight the substantial pressure-loss penalties accompanying the heat-transfer enhancement achieved with the investigated rib geometries. Nevertheless, as shown by the PEC and PEC_h results, h4w3s1 remains the best-performing configuration within the investigated parameter range according to the adopted performance-evaluation criteria, despite exhibiting the highest pressure drop.

5. Conclusions

A three-dimensional numerical investigation was conducted to assess the thermohydraulic performance of a silicon microchannel heat sink equipped with novel staggered triangular ribs whose triangular cross-section is defined in the plane transverse to the mean flow direction. Laminar water flow was investigated over $100 \leq \mathrm{Re} \leq 400$, considering rib shape, width, height, and streamwise spacing. The numerical methodology was supported by grid-independence analysis, validation against published smooth- and ribbed-microchannel data, and verification of the periodic-domain approach.

The initial comparison between rectangular and triangular ribs at the same frontal-area blockage ratio showed that rib shape significantly affects the balance between heat-transfer enhancement and hydraulic penalty. The rectangular rib provided slightly better overall performance up to Re = 200, whereas the transverse-section triangular rib became

increasingly advantageous at higher Reynolds numbers, reaching a PEC 8.7% higher than that of the rectangular configuration at Re = 400.

Increasing either the width or height of the triangular ribs enhanced heat transfer by strengthening flow redistribution, separation, recirculation, and thermal-boundary-layer disruption, although at the expense of increased hydraulic resistance. Within the investigated ranges, increasing rib width produced a stronger thermohydraulic enhancement than increasing rib height, and the full-height configuration h4w3s1 achieved the highest PEC and PEC_h among the width- and height-variation cases.

Comparison of configurations at matched frontal-area blockage ratios further demonstrated that blockage ratio alone is insufficient to characterize rib performance. At BR = 37.5% and Re = 400, the full-height/variable-width configuration produced a 55.3% higher Nusselt number and a 30.7% higher PEC than the corresponding full-width/variable-height configuration.

The complementary indicators Nu_h and PEC_h, based on the heated-base temperature, generally confirmed the performance trends obtained using the conventional definitions, indicating that the main conclusions are also retained when the thermal effectiveness is evaluated with reference to the heated surface.

Rib spacing provided an additional strong influence on performance. For the h4w3s* configuration family, reducing the spacing from 0.40 to 0.20 mm increased the PEC from 1.37 to 2.40 at Re = 400, although the Fanning friction factor simultaneously increased from 0.118 to 0.279. Thus, more frequent rib-induced flow disturbance improves the overall thermohydraulic performance within the investigated range, but with a substantial pressure-loss penalty.

The additional three-dimensional reverse flow analysis showed that, for h4w3s1, the reverse flow volume fraction reaches a maximum at Re = 200 and subsequently decreases, while the reverse flow intensity index increases continuously. This indicates a reorganization of the reverse axial flow accompanying the non-monotonic friction-factor behaviour. Furthermore, the field-synergy analysis revealed a correlation between larger values of the cosine of the global effective synergy angle and higher Nusselt number enhancement ratios.

Overall, the results demonstrate that the performance of transverse-section triangular ribs is governed not only by the magnitude of flow obstruction, but also by its distribution within the channel cross-section and by the frequency of rib-induced disturbance. These findings offer valuable design guidance for compact and efficient MCHS in laminar flow applications, such as in electronics cooling and microscale thermal-management systems.

Author Contributions: Conceptualization, H.M., C.N., E.G.F. and S.S.; methodology, H.M., C.N. and S.S.; validation, H.M.; formal analysis, C.N. and S.S.; investigation, H.M., C.N. and S.S.; resources, H.M., C.N., E.G.F. and S.S.; data curation, H.M., C.N. and S.S.; writing—original draft preparation, H.M.; writing—review and editing, H.M. and S.S.; visualization, H.M. and S.S.; supervision, H.M., C.N., E.G.F. and S.S. All authors have read and agreed to the published version of the manuscript.

Funding: This research received no external funding.

Institutional Review Board Statement: Not applicable.

Informed Consent Statement: Not applicable.

Data Availability Statement: The data presented in this study are available from the corresponding author upon reasonable request.

Acknowledgments: During the preparation of this manuscript, the authors used DeepL (https://www.deepl.com, accessed on 26 October 2026) and ChatGPT-5 Edu for language editing and assistance with manuscript organization and wording. The authors have reviewed and edited the output and take full responsibility for the content of this publication.

Conflicts of Interest: The authors declare no conflicts of interest.

Nomenclature

A_{ch}	unobstructed channel cross-sectional area [m^2]
A_h	heated-wall area [m^2]
A_{rib}	projected frontal rib area [m^2]
A_{sf}	total fluid–solid heat-transfer interface area [m^2]
BR	frontal-area blockage ratio [%]
C_{pf}	specific heat capacity of the fluid [J/(kg K)]
D_h	hydraulic diameter [m]
e_f	friction-factor relative percentage error [%]
e_{Nu}	Nusselt number relative percentage error [%]
f	Fanning friction factor [−]
h	rib height [m]
H	heat sink height [m]
H_{ch}	microchannel height [m]
$\mathcal{H}$	Heaviside function [−]
I_{rev}	reverse flow intensity index [%]
k_f	fluid thermal conductivity [W/(m K)]
k_s	solid thermal conductivity [W/(m K)]
L	microchannel length [m]
L_{per}	periodic module length [m]
p	static pressure [Pa]
Nu	Nusselt number [−]
Nu_h	overall Nusselt number [−]
PEC	performance-evaluation criterion based on α[−]
PEC_h	performance-evaluation criterion based on α_h[−]
q_h	applied wall heat flux [W/m^2]
R_{rev}	reverse flow volume fraction [%]
Re	Reynolds number [−]
s	rib spacing [m]
T	temperature [K]
t_{rib}	streamwise rib thickness [m]
T_b	representative bulk temperature [K]
T_{sf}	mean temperature of the solid–fluid interface [K]
T_h	mean temperature of the heated base [K]
u_a	axial (streamwise) velocity component [m/s]
u_m	mean fluid velocity [m/s]
$\boldsymbol{u}$	velocity vector [m/s]
w	rib width [m]
W	heat sink width [m]
W_{ch}	microchannel width [m]
Δp	pressure drop [Pa]
Δp_{per}	pressure drop in a periodic module [Pa]
Greek symbols:	
α	convective heat-transfer coefficient [$W/(m^2\ K)$]
α_h	overall heat-transfer coefficient [$W/(m^2\ K)$]
β	local synergy angle [°]
β_m	domain integration mean synergy angle [°]
μ_f	dynamic viscosity of the fluid [Pa s]
ρ_f	density of the fluid [kg/m^3]
Ω	total volume of the fluid domain [m^3]
Subscripts:	
0	smooth microchannel
ch	channel
f	fluid
h	heated surface
per	periodic
s	solid

Abbreviations:

GCI	Grid Convergence Index
MCHS	Microchannel Heat Sink

References

1. Sharma, M.K.; Ramos-Alvarado, B. Thermal Management of 3-D Heterogeneously Integrated Microelectronics: Challenges and Future Research Directions. *Commun. Eng.* **2026**, *5*, 28. [CrossRef] [PubMed]
2. Yu, Z.-Q.; Li, M.-T.; Cao, B.-Y. A Comprehensive Review on Microchannel Heat Sinks for Electronics Cooling. *Int. J. Extrem. Manuf.* **2024**, *6*, 022005. [CrossRef]
3. Garimella, S.V.; Fleischer, A.S.; Murthy, J.Y.; Keshavarzi, A.; Prasher, R.; Patel, C.; Bhavnani, S.H.; Venkatasubramanian, R.; Mahajan, R.; Joshi, Y.; et al. Thermal Challenges in Next-Generation Electronic Systems. *IEEE Trans. Compon. Packag. Technol.* **2008**, *31*, 801–815. [CrossRef]
4. Tuckerman, D.B.; Pease, R.F.W. High-Performance Heat Sinking for VLSI. *IEEE Electron Device Lett.* **1981**, *2*, 126–129. [CrossRef]
5. Kandlikar, S.G.; Grande, W.J. Evolution of Microchannel Flow Passages—Thermohydraulic Performance and Fabrication Technology. *Heat Transf. Eng.* **2003**, *24*, 3–17. [CrossRef]
6. Kang, Y.; Luo, Z.; Deng, X.; Zhu, Y.; Xia, Z.; Cheng, P. Research Progress on Microchannel Enhanced Heat Transfer Technology: Passive Methods. *Renew. Sustain. Energy Rev.* **2025**, *224*, 116089. [CrossRef]
7. Wang, Q.; Tao, J.; Cui, Z.; Zhang, T.; Chen, G. Passive Enhanced Heat Transfer, Hotspot Management and Temperature Uniformity Enhancement of Electronic Devices by Micro Heat Sinks: A Review. *Int. J. Heat Fluid Flow* **2024**, *107*, 109368. [CrossRef]
8. Khan, M.Z.U.; Uddin, E.; Akbar, B.; Akram, N.; Naqvi, A.A.; Sajid, M.; Ali, Z.; Younis, M.Y.; García Márquez, F.P. Investigation of Heat Transfer and Pressure Drop in Microchannel Heat Sink Using Al_2O_3 and ZrO_2 Nanofluids. *Nanomaterials* **2020**, *10*, 1796. [CrossRef] [PubMed]
9. Sadiq Al-Baghdadi, M.A.R.; Noor, Z.M.H.; Zeiny, A.; Burns, A.; Wen, D. CFD Analysis of a Nanofluid-Based Microchannel Heat Sink. *Therm. Sci. Eng. Prog.* **2020**, *20*, 100685. [CrossRef]
10. Pan, M.; Wang, H.; Zhong, Y.; Fang, T.; Zhong, X. Numerical Simulation of the Fluid Flow and Heat Transfer Characteristics of Microchannel Heat Exchangers with Different Reentrant Cavities. *Int. J. Numer. Methods Heat Fluid Flow* **2019**, *29*, 4334–4348. [CrossRef]
11. Kumar, K.; Kumar, P. Effect of Groove Depth on Hydrothermal Characteristics of the Rectangular Microchannel Heat Sink. *Int. J. Therm. Sci.* **2021**, *161*, 106730. [CrossRef]
12. Saha, S.; Alam, T.; Siddiqui, M.I.H.; Kumar, M.; Ali, M.A.; Gupta, N.K.; Dobrotă, D. Analysis of Microchannel Heat Sink of Silicon Material with Right Triangular Groove on Sidewall of Passage. *Materials* **2022**, *15*, 7020. [CrossRef] [PubMed]
13. Chai, L.; Xia, G.; Wang, L.; Zhou, M.; Cui, Z. Heat Transfer Enhancement in Microchannel Heat Sinks with Periodic Expansion–Constriction Cross-Sections. *Int. J. Heat Mass Transf.* **2013**, *62*, 741–751. [CrossRef]
14. Vasilev, M.P.; Abiev, R.S.; Kumar, R. Effect of Circular Pin-Fins Geometry and Their Arrangement on Heat Transfer Performance for Laminar Flow in Microchannel Heat Sink. *Int. J. Therm. Sci.* **2021**, *170*, 107177. [CrossRef]
15. Jia, Y.; Huang, J.; Wang, J.; Li, H. Heat Transfer and Fluid Flow Characteristics of Microchannel with Oval-Shaped Micro Pin Fins. *Entropy* **2021**, *23*, 1482. [CrossRef] [PubMed]
16. Ali, N.; Srivastava, S.; Haque, I.; Yadav, J.; Alam, T.; Siddiqui, T.U.; Siddiqui, M.I.H.; Cuce, E. Heat Dissipation and Fluid Flow in Micro-Channel Heat Sink Equipped with Semi-Elliptical Pin-Fin Structures: A Numerical Study. *Int. Commun. Heat Mass Transf.* **2024**, *155*, 107492. [CrossRef]
17. Li, F.; Ma, Q.; Xin, G.; Zhang, J.; Wang, X. Heat Transfer and Flow Characteristics of Microchannels with Solid and Porous Ribs. *Appl. Therm. Eng.* **2020**, *178*, 115639. [CrossRef]
18. Ali, S.; Ahmad, F.; Akhtar, K.; Habib, N.; Aamir, M.; Giasin, K.; Vafadar, A.; Pimenov, D.Y. Numerical Investigation of Microchannel Heat Sink with Trefoil Shape Ribs. *Energies* **2021**, *14*, 6764. [CrossRef]
19. Ali, S.; Habib, N.; Ahmad, F.; Sharif, A.; Vafadar, A. Performance Investigation of Microchannel Heat Sink with Biomimetic Trefoil Cavities on Different Walls. *Int. J. Therm. Sci.* **2026**, *219*, 110225. [CrossRef]
20. Akhtar, K.; Ali, H.; Ud Din, I.; Abbas, A.; Zahir, M.Z.; Ahmad, F.; Alam, F.; Shah, N.; Aamir, M. Heat Transfer Augmentation and Entropy Generation Analysis of Microchannel Heat Sink (MCHS) with Symmetrical Ogive-Shaped Ribs. *Energies* **2023**, *16*, 2783. [CrossRef]
21. Ali, S.; Ahmad, F.; Hassan, M.; Rehman, Z.; Wadood, A.; Ahmad, K.; Park, H. Thermo-Fluid Characteristics of Microchannel Heat Sink with Multi-Configuration NACA 2412 Hydrofoil Ribs. *IEEE Access* **2021**, *9*, 128407–128416. [CrossRef]

22. Xu, J.; Jiang, R.; Lian, J.; Zhang, T. Shark-Scale Inspired Gradient Airfoil Ribs for Synergistic Enhancement of Heat Transfer and Reduction of Flow Resistance in Microchannel Heat Sinks. *Int. Commun. Heat Mass Transf.* **2026**, *180*, 112432. [CrossRef]
23. Li, B.; Cui, Y.; Li, G.; Jiang, H. Numerical Analysis on Thermal-Hydraulic Performance of Optimized Microchannel Heat Sink with Slant Ribs and Quatrefoil Rib-Elliptical Groove Complex Structures. *Appl. Therm. Eng.* **2024**, *240*, 122165. [CrossRef]
24. Dash, A.P.; Alam, T.; Siddiqui, M.I.H.; Blecich, P.; Kumar, M.; Gupta, N.K.; Ali, M.A.; Yadav, A.S. Impact on Heat Transfer Rate Due to an Extended Surface on the Passage of Microchannel Using Cylindrical Ribs with Varying Sector Angle. *Energies* **2022**, *15*, 8191. [CrossRef]
25. Ali, N.; Haque, I.; Alam, T.; Siddiqui, T.U.; Ansari, M.A.; Yadav, J.; Srivastava, S.; Cuce, E.; Ashraf, I.; Dobrotă, D. Numerical Investigation on Heat Transfer and Flow Mechanism in Microchannel Heat Sink Having V Shape Ribs. *Case Stud. Therm. Eng.* **2025**, *65*, 105684. [CrossRef]
26. Wang, D.; Xue, L.; Liu, C.; Chen, H.; Xia, C.; Qian, Q.; Cheng, L. Effects of Staggered Truncated Ribs on Thermal-Hydraulic Performance and Entropy Generation of Microchannel Heat Sinks. *Case Stud. Therm. Eng.* **2025**, *65*, 105597. [CrossRef]
27. Kumari, N.; Alam, T.; Ali, M.A.; Yadav, A.S.; Gupta, N.K.; Siddiqui, M.I.H.; Dobrotă, D.; Rotaru, I.M.; Sharma, A. A Numerical Investigation on Hydrothermal Performance of Micro Channel Heat Sink with Periodic Spatial Modification on Sidewalls. *Micromachines* **2022**, *13*, 1986. [CrossRef] [PubMed]
28. Zhao, H.; Ma, H.; Yan, X.; Yu, H.; Xiao, Y.; Xiao, X.; Liu, H. Investigation of Hydrothermal Performance in Micro-Channel Heat Sink with Periodic Rectangular Fins. *Micromachines* **2023**, *14*, 1818. [CrossRef] [PubMed]
29. Wang, G.-L.; Yang, D.-W.; Wang, Y.; Niu, D.; Zhao, X.-L.; Ding, G.-F. Heat Transfer and Friction Characteristics of the Microfluidic Heat Sink with Variously-Shaped Ribs for Chip Cooling. *Sensors* **2015**, *15*, 9547–9562. [CrossRef] [PubMed]
30. Chai, L.; Wang, L. Thermal-Hydraulic Performance of Interrupted Microchannel Heat Sinks with Different Rib Geometries in Transverse Microchambers. *Int. J. Therm. Sci.* **2018**, *127*, 201–212. [CrossRef]
31. Wang, W.; Li, Y.; Zhang, Y.; Li, B.; Sundén, B. Analysis of Laminar Flow and Heat Transfer in an Interrupted Microchannel Heat Sink with Different Shaped Ribs. *J. Therm. Anal. Calorim.* **2020**, *140*, 1259–1266. [CrossRef]
32. Wong, K.-C.; Lee, J.-H. Investigation of Thermal Performance of Microchannel Heat Sink with Triangular Ribs in the Transverse Microchambers. *Int. Commun. Heat Mass Transf.* **2015**, *65*, 103–110. [CrossRef]
33. Chai, L.; Wang, L.; Bai, X. Thermohydraulic Performance of Microchannel Heat Sinks with Triangular Ribs on Sidewalls—Part 1: Local Fluid Flow and Heat Transfer Characteristics. *Int. J. Heat Mass Transf.* **2018**, *127*, 1124–1137. [CrossRef]
34. Chai, L.; Wang, L.; Bai, X. Thermohydraulic Performance of Microchannel Heat Sinks with Triangular Ribs on Sidewalls—Part 2: Average Fluid Flow and Heat Transfer Characteristics. *Int. J. Heat Mass Transf.* **2019**, *128*, 634–648. [CrossRef]
35. Chen, Z.; Feng, Z.; Zhang, Q.; Zhang, J.; Guo, F. Effects of Regular Triangular Prisms on Thermal and Hydraulic Characteristics in a Minichannel Heat Sink. *Int. J. Heat Mass Transf.* **2022**, *188*, 122583. [CrossRef]
36. Feng, Z.; Zhou, C.; Guo, F.; Zhang, J.; Zhang, Q.; Li, Z. The Effects of Staggered Triangular Ribs Induced Vortex Flow on Hydrothermal Behavior and Entropy Generation in Microchannel Heat Sink. *Int. J. Therm. Sci.* **2023**, *191*, 108331. [CrossRef]
37. Alnaimat, F.; Rahhal, A.A.E.H.; Mathew, B.; Berrouk, A. Fluid Flow and Heat Transfer Investigation of Microchannel Heat Sink with Sidewall Triangle Ribs. *Int. J. Thermofluids* **2025**, *26*, 101141. [CrossRef]
38. Shamsoddini Lori, M.; Vafai, K. Heat Transfer and Fluid Flow Analysis of Microchannel Heat Sinks with Periodic Vertical Porous Ribs. *Appl. Therm. Eng.* **2022**, *205*, 118059. [CrossRef]
39. Han, J.C.; Glicksman, L.R.; Rohsenow, W.M. An Investigation of Heat Transfer and Friction for Rib-Roughened Surfaces. *Int. J. Heat Mass Transf.* **1978**, *21*, 1143–1156. [CrossRef]
40. Ling, C.-M.; Jin, Y.-Y.; Chen, Z.-Q. Heat/Mass Transfer and Pressure Drop in a Triangular-Rib-Roughened Rectangular Channel. *Int. J. Heat Fluid Flow* **1994**, *15*, 486–490. [CrossRef]
41. Ahn, S.W. The Effects of Roughness Types on Friction Factors and Heat Transfer in Roughened Rectangular Duct. *Int. Commun. Heat Mass Transf.* **2001**, *28*, 933–942. [CrossRef]
42. Webb, R.L. Performance Evaluation Criteria for Use of Enhanced Heat Transfer Surfaces in Heat Exchanger Design. *Int. J. Heat Mass Transf.* **1981**, *24*, 715–726. [CrossRef]
43. Wang, Z.; Yin, Y.; Yang, L.; Wang, Y.; Luan, Y. Similar Characteristics of Heat Transfer in Different Scale Cooling Channel with Ribs. *Heat Transf. Eng.* **2022**, *43*, 1025–1040. [CrossRef]
44. ANSYS, Inc. *ANSYS Fluent User's Guide, Release 2025 R1*; ANSYS, Inc.: Canonsburg, PA, USA, 2025.
45. Liu, X.; Chen, L.; Peng, M.; Ji, W.-T.; Tao, W.-Q. Topology optimization of the manifold microchannels with triple-objective functions. *Numer. Heat Transf. Part B Fundam.* **2021**, *80*, 89–114. [CrossRef]
46. He, Y.L.; Tao, W.Q. Numerical studies on the inherent interrelationship between field synergy principle and entransy dissipation extreme principle for enhancing convective heat transfer. *Int. J. Heat Mass Transf.* **2014**, *74*, 196–205. [CrossRef]
47. Roache, P.J. Perspective: A Method for Uniform Reporting of Grid Refinement Studies. *J. Fluids Eng.* **1994**, *116*, 405–413. [CrossRef]

48. Mokhtari, A.; Corso, P.; Jung, B.; Ferrari, L.; Zheng, S.; Obrist, D. Comparison of 4D Flow MRI and Computational Fluid Dynamics in Carotid Models with Different Stenosis Levels. *Comput. Biol. Med.* **2025**, *194*, 110405. [CrossRef] [PubMed]
49. Nilsson, F.; Emendi, M.; Broman, L.M.; Prahl Wittberg, L. Protruding Objects in the Membrane Lung Outlet May Increase Thrombogenicity: Fluid Dynamical Insights. *ASAIO J.* **2026**, *72*, 411–417. [CrossRef] [PubMed]

Disclaimer/Publisher's Note: The statements, opinions and data contained in all publications are solely those of the individual author(s) and contributor(s) and not of MDPI and/or the editor(s). MDPI and/or the editor(s) disclaim responsibility for any injury to people or property resulting from any ideas, methods, instructions or products referred to in the content.